

Stabilizing Consistency Training: A Flow Map Analysis and Self-Distillation

Youngjoong Kim¹ Duhoе Kim² Woosung Kim¹ Jaesik Park¹

Abstract

Consistency models have been proposed for fast generative modeling, achieving results competitive with diffusion and flow models. However, these methods exhibit inherent instability and limited reproducibility when training from scratch, motivating subsequent work to explain and stabilize these issues. While these efforts have provided valuable insights, the explanations remain fragmented, and the theoretical relationships remain unclear. In this work, we provide a theoretical examination of consistency models by analyzing them from a flow map-based perspective. This joint analysis clarifies how training stability and convergence behavior can give rise to degenerate solutions. Building on these insights, we revisit self-distillation as a practical remedy for certain forms of suboptimal convergence and reformulate it to avoid excessive gradient norms for stable optimization. We further demonstrate that our strategy extends beyond image generation to diffusion-based policy learning, without reliance on a pretrained diffusion model for initialization, thereby illustrating its broader applicability.

1. Introduction

Diffusion (Song & Ermon, 2019; 2020; Ho et al., 2020; Song et al., 2021) and flow matching models (Liu et al., 2023; Lipman et al., 2023) have achieved remarkable performance across a wide range of applications. This progress stems from flow-based modeling and multi-step inference, but is limited by multiple network evaluations during generation.

Consistency Models (Song et al., 2023) and its variants (Frans et al., 2025; Geng et al., 2025a; Peng et al., 2025) have been proposed for training from scratch in few-step generation. Earlier studies on consistency models have often exhibited training instability and limited reproducibil-

¹Department of Computer Science and Engineering, Seoul National University, Seoul, Republic of Korea ²School of Computer Science and Engineering, Chung-Ang University, Seoul, Republic of Korea. Correspondence to: Jaesik Park <jaesik.park@snu.ac.kr>.

ity, motivating subsequent work to stabilize training (Song & Dhariwal, 2024; Geng et al., 2025c; Lu & Song, 2025). While prior efforts have provided meaningful insights, the explanations remain fragmented, and the theoretical relationships among existing approaches remain unclear.

Prior work has explored distillation-based perspectives on consistency models from complementary viewpoints. Boffi et al. (2025b) formulates Eulerian distillation and highlights discrepancies between distillation and training-from-scratch objectives, with a primary focus on understanding distillation behavior. Sabour et al. (2025) further introduces a consistency-based reformulation of Eulerian distillation, demonstrating its scalability in teacher-student settings.

Self-distillation (Boffi et al., 2025a) further considers training from scratch by learning flows while distilling from the model itself using Eulerian distillation. Although this provides a connection between distillation and training-from-scratch, large gradient norms have been reported in high-dimensional settings, posing challenges for optimization.

In this work, we present a systematic examination of training instability in consistency models. We jointly analyze existing approaches through two training objectives, Eulerian distillation and consistency training, with key design factors, including time condition and guiding velocity.

This perspective clarifies how distinct objectives lead to different convergence behaviors. First, while prior work has identified mismatches between training objectives, it has not been formally established whether such differences necessarily imply different optima. We address this question by characterizing the optimality conditions of Eulerian distillation. We show that training with conditional velocity can converge to degenerate solutions, whereas training with marginal velocity can yield the desired optimum.

Second, we analyze consistency training by relating it to Eulerian distillation and show how this explains the effects of optimization noise, including small batch sizes, on convergence toward degenerate solutions.

Third, by analyzing the functional gradient of the consistency training objective, we show that its stationary solutions correspond to fixed-point solutions. We demonstrate that the structure and complexity of these fixed points depend on the time condition, as illustrated by empirical loss landscapes.

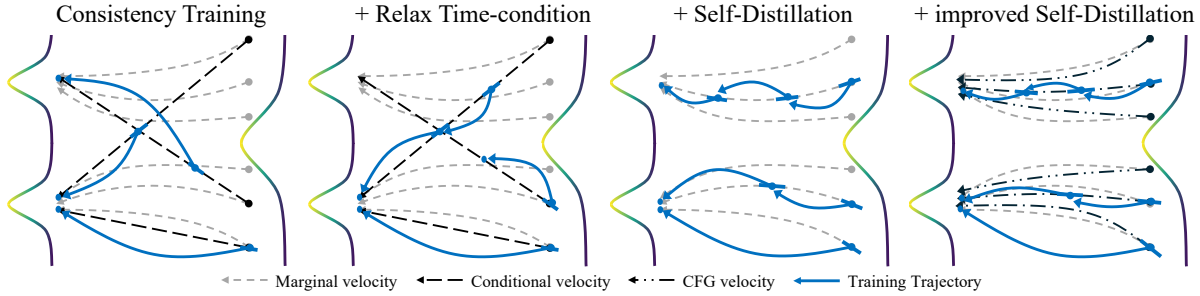


Figure 1. From consistency training to improved Self-Distillation. Consistency training learns a mapping over conditional velocity, often suffering from training instability and reproducibility issues. Relaxing the time condition mitigates this instability, and self-distillation provides a principled target by aligning with the marginal velocity. However, directly applying self-distillation leads to unstable training. We therefore reformulate the objective and incorporate classifier-free guidance, further stabilizing training and improving reproducibility.

Motivated by the analysis, we revisit self-distillation as a practical mechanism for addressing certain forms of suboptimal convergence induced by conditional velocity guidance. Our analysis indicates that training with marginal velocity guidance can yield the desired optimum under these settings. While self-distillation naturally provides this form of marginal guidance, existing formulations are not directly compatible with consistency training because they can induce excessive gradient norms in high-dimensional settings.

Building on the consistency-based reformulation introduced by Sabour et al. (2025), we reformulate the self-distillation objective to constrain gradient magnitudes while preserving its intended guidance. This enables stable optimization in practice and enables effective self-distillation in training-from-scratch settings. Finally, we show that this reformulated objective can be seamlessly combined with classifier-free guidance. We provide an overview of our flow map perspective in Figure 1.

We empirically evaluate our approach on ImageNet-1K 256 × 256 in few-step generation settings. It exhibits stable behavior and achieves performance comparable to that of recent methods without relying on pretrained diffusion models for initialization, thereby supporting the practical relevance of our theoretical insights. We further extend our evaluation to diffusion-based policy learning, demonstrating applicability beyond the image generation domain.

2. Related Work

Diffusion and Flow Matching Models. Diffusion models (Ho et al., 2020; Song & Ermon, 2019; Song et al., 2021) and flow matching models (Albergo & Vanden-Eijnden, 2023; Albergo et al., 2023; Boffi et al., 2025b; Liu et al., 2023) are generative models that gradually transform a tractable noise distribution into the data distribution. These models have achieved remarkable progress in high-fidelity generation (Rombach et al., 2022; Podell et al., 2024; Esser et al., 2024). However, their reliance on a multi-step sam-

pling requires substantial computational resources.

Few-step Generation. Several works have explored improving sampling efficiency of diffusion models (Salimans & Ho, 2022; Xiao et al., 2022; Rombach et al., 2022). These approaches aim to distill pretrained diffusion models into fewer-step generators, adopt GANs, or leverage VAEs to reduce input size. In parallel, score distillation (Yin et al., 2024b;a; Zhou et al., 2024) has been proposed to construct one-step generators, while both rely on additional distillation stages or auxiliary networks, increasing training cost.

Consistency Models. Consistency Models (Song et al., 2023) are designed to predict a sample directly from any point along a flow trajectory. Both distillation and training methods have been proposed, whereas training from scratch can exhibit large loss variance, motivating earlier work on stabilization (Song & Dhariwal, 2024; Geng et al., 2025c; Lu & Song, 2025). Other studies (Issenhuth et al., 2025; Silvestri et al., 2025; Boffi et al., 2025b) have suggested that a discrepancy between distillation and training objectives can lead to high loss variance and suboptimal convergence when training from scratch. To mitigate this, network-induced couplings (Issenhuth et al., 2025; Silvestri et al., 2025) are introduced to reduce loss variance. Self-distillation (Boffi et al., 2025a) learns flows and jointly distills shortcut mappings from its learned flow, while it has been reported to encounter large gradient norms in high-dimensional settings when Eulerian distillation is employed.

Unified Framework. Recently, several studies have aimed to relate flow matching and consistency models. UCGM (Sun et al., 2025) integrates both paradigms, but does not account for the relaxed mapping constraint of arbitrary time points. Boffi et al. (2025b); Kim et al. (2024) present mathematical frameworks for consistency models, defining a model that learns *flow maps* as mappings between any two points on the same trajectory. While these works offer valuable theoretical perspectives, instability mechanisms arising from optimization noise, initialization, or time conditioning are not the primary focus of these analyses.

3. Preliminary

Flow Matching. Given a dataset X with underlying distribution p_X , flow matching models are trained to match the velocity fields of continuous flows, starting from a tractable distribution p_Z . Prior work constructs such flows via an interpolation, $x_t = \alpha_t x + \sigma_t z$, where $x \sim p_X$ and $z \sim p_Z$.

Let α_t and σ_t are continuous and monotone, with $\alpha_0 = \sigma_T = 1$ and $\alpha_T = \sigma_0 = 0$ for $t \in [0, T]$. Under bounded derivatives, a marginal distribution ρ_t induced by the flow satisfies $\rho_0 = p_X$ and $\rho_T = p_Z$. To ensure well-defined convergence of the consistency objective, we assume: $\alpha_t \sigma'_t - \sigma_t \alpha'_t = \nu \neq 0$ for all $t \in [0, T]$, where ν is a constant (see Section A.4). Notably, linear and trigonometric interpolations satisfy this with $\nu = 1$.

With the constructed flow, the flow matching models optimize the squared error between the conditional velocity $v_t(x_t|x) = \alpha'_t x + \frac{\sigma'_t}{\sigma_t} (x_t - \alpha_t x)$ and a network $F_\theta(x_t; t)$:

$$\mathcal{L}_{\text{CFM}} = \mathbb{E}_{x,z,t} [\|F_\theta(x_t; t) - v_t(x_t|x)\|_2^2]. \quad (1)$$

Conditional flow matching \mathcal{L}_{CFM} converges to the flow induced by the marginal velocity $v_t^*(x_t) = \mathbb{E}_{x|x_t} [v(x_t|x)]$. If $v_t^*(x)$ is Lipschitz continuous in both t and x , the ODE $dx_t = v_t^*(x_t)dt$ has a unique solution (Lipman et al., 2023).

Flow Map. From flows defined by interpolation, our goal is to draw samples from the target distribution in a few sampling steps. To this end, we adopt a *flow map* $f_{t,s}(x_t)$ (Kim et al., 2024; Boffi et al., 2025b), which is a mapping between two points x_t and x_s ($s < t$) on the same trajectory:

$$f_{t,s}(x_t) = x_t + \int_t^s v_\tau^*(x_\tau) d\tau = x_s. \quad (2)$$

Training Flow Map. Since the flow map is defined as an integral, direct supervision from scratch is challenging. Recent studies adopt consistency training (Song et al., 2023) to avoid data generation, which can be derived from the Eulerian equation (see Section A.3 and Boffi et al. (2025b)):

$$\partial_t f_{t,s}(x_t) + v_t^*(x_t) \cdot \nabla_x f_{t,s}(x_t) = 0. \quad (3)$$

Note that if f is continuous in t and s , Lipschitz continuous in x , and satisfies the boundary condition $f_{t,t}(x_t) = x_t$, the flow map $f_{t,s}$ is the unique solution to the Eulerian equation.

To train a flow map network $f_\theta = f_\theta(x_t; t, s)$ using this equation, Eulerian distillation (Boffi et al., 2025b) formulates the objective as a squared minimization problem:

$$\mathcal{L}_{\text{ED}} = \mathbb{E}_{x,z,t,s} [\|\partial_t f_\theta + v_t^* \cdot \nabla_x f_\theta\|_2^2], \quad (4)$$

where $v_t^* = v_t^*(x_t)$. This reduces to consistency distillation when $s = 0$ (Song et al. (2023), see Section A.5):

$$\mathcal{L}_{\text{CD}} = \mathbb{E} [\|f_\theta - f_{\theta-} + \partial_t f_{\theta-} + v_t^* \cdot \nabla_x f_{\theta-}\|_2^2], \quad (5)$$

where $f_{\theta-}$ denotes the gradient-detached network. For consistency training from scratch, using $v_t = v_t(x_t|x)$ instead of $v_t^*(x_t)$ is a more common choice:

$$\mathcal{L}_{\text{CT}} = \mathbb{E} [\|f_\theta - f_{\theta-} + \partial_t f_{\theta-} + v_t \cdot \nabla_x f_{\theta-}\|_2^2]. \quad (6)$$

Because \mathcal{L}_{ED} involves a Jacobian-vector product (JVP), its optimization requires second-order differentiation, which introduces computational overhead. On the other hand, consistency training adopts a stop-gradient operation, which avoids this issue. However, it alters gradient dynamics, potentially affecting training stability (Theorem 4.3).

4. Analysis of Instability

In this section, we first analyze instability in consistency models from a flow map perspective, focusing on how different design choices affect convergence properties and optimization dynamics. Based on this analysis, we explain why training from scratch may deviate from the desired flow map in practical settings.

4.1. Flow Map Representation for Analysis

To facilitate a joint analysis of recent consistency models, we adopt a flow map representation to express different training objectives in a common form. This representation serves as an analytical tool rather than a new assumption, and will be used throughout the paper to compare convergence behaviors and training dynamics across methods.

Flow Map Representation. To enable a systematic analysis of training instability in consistency models, we propose a flow map representation for commonly used interpolations, expressed as a one-step Euler solution with a network F_θ :

$$f_\theta(x_t; t, s) = \nu^{-1} (A'_{t,s} x_t - A_{t,s} F_\theta(x_t; t, s)), \quad (7)$$

where $A_{t,s} = \sigma_t \alpha_s - \sigma_s \alpha_t$. Under this representation, UCGM (Sun et al., 2025) can be viewed as a special case with fixed $s = 0$. TM (Shaul et al., 2025) also considers arbitrary (t, s) , and it shares the functional structure under ν -assumption, while differing in parameterization.

With this representation, we propose a joint interpretation of recent consistency models (proof in Section A.5).

Proposition 4.1. *(Interpretation of Recent Methods)* Recent consistency models can be interpreted within the flow map representation, satisfying the following transport equation:

$$\partial_t f_\theta(x_t; t, s) + \tau_t(x_t, x) \cdot \nabla_x f_\theta(x_t; t, s) = 0, \quad (8)$$

where x_t is given by the Interpolant, τ_t by the Trajectory, and t, s by the Timestep, as summarized in Table 1.

Table 1. Summary of recent consistency models interpreted under the flow map representation. *Int.* denotes the interpolant, *Traj.* the guiding trajectory, and *Time* the timestep conditions. $\Phi_t(x_t)$ is the teacher network, $F_\theta(x_t; t, s)$ the training network, and $F_t(x_t)$ denotes $F_\theta(x_t; t, t)$ for brevity. Our method is aligned with the learned marginal velocity and the relaxed time condition, enabled by a reformulation of self-distillation to improve training stability.

MODEL	INT.	TRAJ.	TIME	OBJ.
DISTILLATION-BASED METHODS				
FMM-EMD (BOFFI ET AL., 2025B)	LIN.	$\Phi_t(x_t)$	$s < t$	\mathcal{L}_{ED}
AYF-EMD (SABOUR ET AL., 2025)	LIN.	$\Phi_t(x_t)$	$s < t$	\mathcal{L}_{CD}
SCD (LU & SONG, 2025)	TRI.	$\Phi_t(x_t)$	$s = 0$	\mathcal{L}_{CD}
CONSISTENCY TRAINING METHODS				
MEANFLOW (GENG ET AL., 2025A)	LIN.	$v_t(x_t x)$	$s < t$	\mathcal{L}_{CT}
CONSISTENCYFM (YANG ET AL., 2024)	LIN.	$v_t(x_t x)$	$s = 0$	\mathcal{L}_{CT}
SCT (LU & SONG, 2025)	TRI.	$v_t(x_t x)$	$s = 0$	\mathcal{L}_{CT}
UCGM (SUN ET AL., 2025)	ANY	$v_t(x_t x)$	$s = 0$	\mathcal{L}_{CT}
SELF-DISTILLATION METHODS				
SHORTCUT MODEL (FRANS ET AL., 2025)	LIN.	$F_t(x_t)$	$s < t$	\mathcal{L}_{SD}
ESD (BOFFI ET AL., 2025A)	LIN.	$F_t(x_t)$	$s < t$	\mathcal{L}_{SD}
ISD (OURS)	ANY	$F_t(x_t)$	$s < t$	$\mathcal{L}_{\text{SD-R}}$

4.2. Suboptimality and Instability

Most consistency training approaches learn flow maps guided by a conditional velocity. We refer to Eulerian distillation under a conditional velocity field as *direct training*.

$$\mathcal{L}_{\text{DT}} = \mathbb{E} [\|\partial_t f_\theta + v(x_t|x) \cdot \nabla_x f_\theta\|_2^2]. \quad (9)$$

Due to the gap between conditional and marginal velocity, we show that direct training does not guarantee convergence to the marginal flow map (proof in Section A.6).

Proposition 4.2. *(Optimality condition of direct training)*
The optimum of direct training is attained when

$$\mathcal{L}_{\text{ED}} + C = 0, \quad C = \nabla \cdot (\Sigma_{\Delta v|x_t} \nabla_x f_\theta), \quad (10)$$

where $\Delta v = v_t(x_t|x) - v_t^*(x_t)$ and $\Sigma_{\Delta v|x_t}$ is the conditional covariance $\text{Cov}_{x|x_t}[\Delta v]$.

This suggests that training can result in a degenerate flow map ($\mathcal{L}_{\text{ED}} > 0$ with $C < 0$), which is a suboptimal solution.

To demonstrate the suboptimality of direct training, we conduct experiments on a toy dataset, as shown in Figure 2. Compared to Eulerian distillation, which successfully learns the ground-truth distribution, direct training converges to a degenerate distribution, consistent with the proposition.

Instead, we show that consistency training can recover solutions satisfying the Eulerian equation, even when guided by conditional velocity. However, this does not imply convergence due to its gradient dynamics (see Section A.7).

Proposition 4.3. *(Instability of consistency training)* Consistency training with a conditional velocity admits fixed-point solutions that satisfy the Eulerian equation. However, it lacks the sufficient second-order structure required for

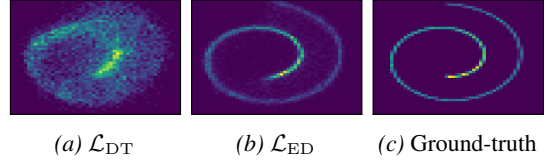


Figure 2. Toy experiments with a 5-layer MLP (batch size of 2048). \mathcal{L}_{DT} drives flow map training toward a suboptimal solution, while \mathcal{L}_{ED} leads to a solution close to the ground-truth.

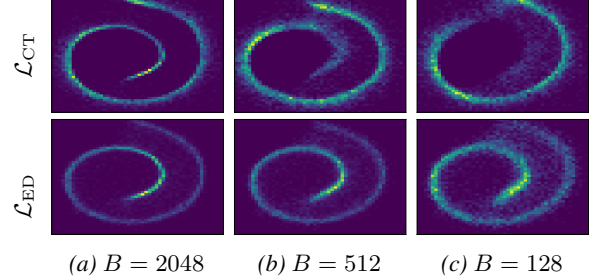


Figure 3. Consistency training (with \mathcal{L}_{CT}) is biased toward degenerate distributions when the batch size B decreases.

convergence and only ensures the existence of such fixed points. As a result, it may fail to converge.

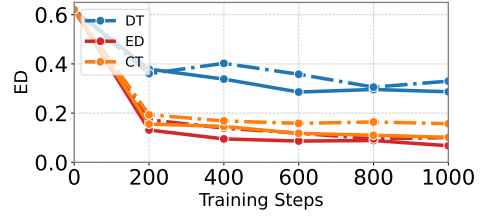


Figure 4. \mathcal{L}_{ED} over training steps on a toy dataset. The experiment follows Figure 2, except for the batch size (solid lines indicate a batch size of 2048, and dash-dot lines indicate 128).

Since this connection to the Eulerian equation holds *only at the expectation level*, a small batch size shifts the optimization closer to direct training. As shown in Figure 3, this can lead to a degenerate solution and helps explain why recent consistency models use large batch sizes.

As shown in Figure 4, we also measure \mathcal{L}_{ED} for the toy dataset, which serves as a proxy for estimating the optimality of flow maps. While it does not fully reflect generation performance, consistency training with small batch sizes and direct training yield higher \mathcal{L}_{ED} values, which can be interpreted as a signal of a degenerate solution.

This proposition can also help explain why performance degrades in some cases of continued training: models can escape the optimum and drift toward undesired fixed points due to the lack of curvature around it.

Weight Initializations. We further observe that the performance of consistency models with $s = 0$ is sensitive to weight initialization, and in some cases, does not reach the desired optima. In practice, recent consistency models

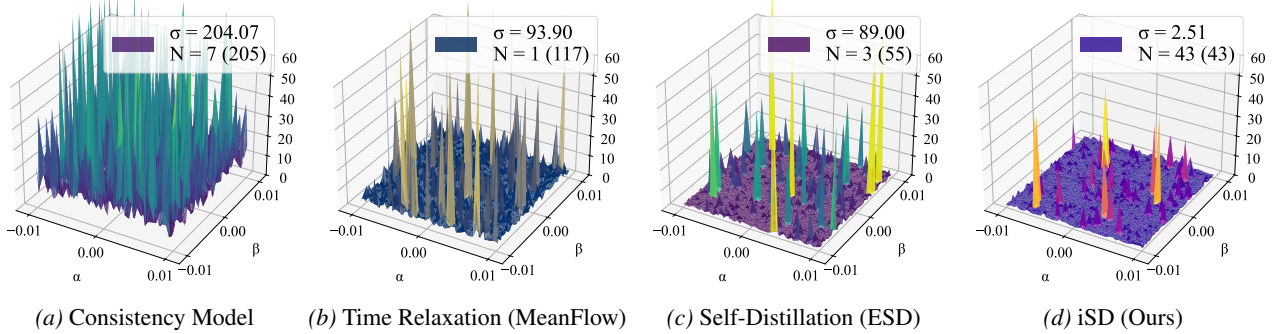


Figure 5. Loss landscapes of four methods. α and β denote the top-2 eigenvectors of the Hessian on ImageNet-1K with DiT-B/4. σ denotes the standard deviations of each landscape, and N the number of samples outside each method’s own 95% confidence bound. Values in parentheses report the number of samples exceeding the 95% bound defined by iSD, as a common reference (details in Section C.6).

Table 2. Consistency training results under different preconditioners. *Preconditioner FID* denotes the FIDs of pretrained networks for given ODE solver and sampling-step pairs. *2-FID* denotes two-step FIDs of consistency models initialized from the corresponding preconditioner (details in Section C.1).

PRECONDITIONER	PRECONDITIONER FID \downarrow	2-FID \downarrow
MULTI-STEP BASELINE	1.21 (UCGM-S, 30-STEP)	2.52
LIGHTNINGDiT	2.17 (EULER, 250-STEP)	9.59
IN-HOUSE FLOW MODEL	2.41 (UCGM-S, 30-STEP)	5.78
W/O PRECONDITIONER	-	419.60
REPORTED BASELINE	1.21 (UCGM-S, 30-STEP)	1.42

rely on initialization with pretrained diffusion models, often referred to as a *preconditioner*. We find that performance varies with the choice of preconditioner.

As shown in Table 2, we evaluated an open-source consistency model (Sun et al., 2025) on ImageNet-1K 256×256 . With the baseline preconditioner, the model achieves results comparable to those reported. However, when using the other pretrained flow model, the FIDs become worse.

The resulting few-step FIDs are inconsistent: stronger preconditioners do not necessarily yield better consistency models. Additionally, models diverge when initialized randomly, suggesting that the optimum is inaccessible in this case.

This can be understood from Theorem 4.3: initialization matters because training is driven toward nearby fixed points rather than the global optimum. Without the known preconditioner, the training becomes difficult to reproduce.

Linearization Cost Hypothesis. Some studies (Geng et al., 2025a; Frans et al., 2025) enable training from scratch without a preconditioner. The key difference is that they allow $s < t$, while others fix $s = 0$. Intuitively, training long-range mappings is more challenging than short-range ones, since the linearization error increases with step size.

In both objectives, $s \rightarrow t$ amplifies the flow matching term, while $s \rightarrow 0$ amplifies a linearization term involving JVP.

It is structurally more complex and can give rise to more undesired fixed points (Section A.9). We hypothesize that fixing $s = 0$ makes optimization less stable, while relaxing to $s < t$ balances the terms and mitigates instability.

To support our hypothesis, we examine the loss landscapes of each objective, as shown in Figure 5. This indicates that time relaxation reduces loss variance and spikes, supporting our claim. The method in the next section (iSD) produces even smoother landscapes, resulting in more stable training.

Summary. As consistency training coincides with Eulerian distillation only in expectation, small batch sizes shift training closer to direct training, which can result in degenerate solutions (Theorem 4.2). Since the objective only ensures fixed-point solutions (Theorem 4.3), performance becomes sensitive to initialization, and this sensitivity is mitigated when the time condition is relaxed to $s < t$.

As a practical consequence, these instability mechanisms reveal limited reproducibility across initializations and training settings. Motivated by this observation, we seek to improve reproducibility by eliminating reliance on preconditioners through time-condition relaxation and reducing bias from direct training via marginal velocity guidance.

5. Method

From Table 1, we identify that Eulerian Self-Distillation (ESD; Boffi et al. (2025a)) is guided by the marginal velocity under a relaxed time condition. It can make random initialization feasible, reducing the need for preconditioners. However, ESD exhibits large gradient norms on high-dimensional data, which destabilizes training.

Since ESD is not intended to explicitly address the training stability of existing consistency models, we build on the consistency-based formulation of Sabour et al. (2025) and reformulate self-distillation to be compatible with these models. This reformulation is designed to improve training stability and reproducibility.

We further show that this formulation can be seamlessly combined with classifier-free guidance, yielding additional performance gains. We call this approach ***improved Self-Distillation (iSD)***.

5.1. Eulerian Self-Distillation

ESD trains $F_\theta(x_t; t, t)$ via flow matching, while jointly optimizing Eulerian equation for $f_\theta(x_t; t, s)$ guided by itself:

$$\mathcal{L}_{\text{SD}} = \mathbb{E} [\|\partial_t f_\theta + F_\theta - (x_t; t, t) \cdot \nabla_x f_\theta\|_2^2]. \quad (11)$$

This objective encourages convergence to the marginal flow map, addressing suboptimality (see Section B.1).

5.2. improved Self-Distillation (iSD)

Reformulation. To enable ESD while incorporating design choices, we propose to reformulate self-distillation \mathcal{L}_{SD} using the flow map representation (Equation (7)). In this case, the guidance velocity $v_\theta = F_\theta(x_t; t, t)$ corresponds to the marginal velocity under joint training of flow matching:

$$\mathcal{L}_{\text{SD}} = \mathbb{E} \left[\left\| A''_{t,s} x_t + A'_{t,s} (v_\theta - F_\theta) - A_{t,s} \frac{dF_\theta}{dt} \right\|_2^2 \right] \quad (12)$$

where $F_\theta = F_\theta(x_t; t, s)$. To reduce gradient norms, we consider two stop-gradient placements: only the spatial derivative and the full derivative. Both yield theoretically well-defined objectives admitting the desired fixed points (Theorem 4.3), and we empirically select the latter for improved training stability and efficiency (see Section A.7):

$$\mathcal{L}_{\text{SD-R}} = \mathbb{E} [\|F_\theta - \text{sg}[F_{\text{tgt}}]\|_2^2], \quad (13)$$

$$F_{\text{tgt}} = F_\theta + A''_{t,s} x_t + A'_{t,s} (v_\theta - F_\theta) - A_{t,s} \frac{dF_\theta}{dt}. \quad (14)$$

Thus, our final objective, improved Self-distillation, follows:

$$\mathcal{L}_{\text{iSD}} = \lambda_1 \mathcal{L}_{\text{CFM}} + \lambda_2 \mathcal{L}_{\text{SD-R}}, \quad (15)$$

$$\mathcal{L}_{\text{CFM}} = \mathbb{E} [\|F_\theta(x_t; t, t) - v_t(x_t|x)\|_2^2]. \quad (16)$$

Following Theorem 4.3, although consistency training ensures the marginal flow map at its fixed point, incorporating self-distillation can further reduce loss variance and stabilize training (details in Section B.2).

Computing JVP. To consistently align with the marginal velocity, dF_θ/dt needs to follow $dF_\theta/dt = \partial_t F_\theta + v_\theta \cdot \nabla_x F_\theta$. This can be implemented using standard JVP APIs with inputs (x_t, t, s) and tangents $(v_\theta, 1, 0)$. This differs from prior consistency models, which assume tangents $(v_t(x_t|x), 1, 0)$.

Alternatively, we can approximate it using a finite difference. Given a small step ϵ , we define displaced inputs to $\hat{x}_{t\pm\epsilon} = x_t \pm \epsilon \cdot v_\theta$, and approximate $dF_\theta/dt \approx [F_\theta(\hat{x}_{t+\epsilon}; t+\epsilon, s) - F_\theta(\hat{x}_{t-\epsilon}; t-\epsilon, s)]/(2\epsilon)$, where s is held fixed.

Classifier-free Guidance. Classifier-free Guidance (CFG) is a widely used technique for improving diffusion models. However, since flow maps parameterize mappings rather than velocities, directly applying CFG does not guarantee mappings along the CFG velocity (see Section B.4).

This motivates two extensions of self-distillation: *Post-CFG* and *Pre-CFG*. Post-CFG operates as a classical CFG:

$$F_\emptyset = F_\theta(x_t; t, s, \emptyset), \quad F_c = F_\theta(x_t; t, s, c), \quad (17)$$

$$\tilde{F}_c = F_\emptyset + \omega(F_c - F_\emptyset), \quad (18)$$

$$\tilde{f}_\theta(x_t; t, s, c) = \nu^{-1}(A'_{t,s} x_t - A_{t,s} \tilde{F}_c), \quad (19)$$

where \emptyset is the null class label, c is the class label, and ω is the guidance scale. Although this formulation is not guaranteed to follow the CFG velocity field, it can be readily applied after training.

To ensure that the flow map follows the CFG field, we introduce a training-time CFG formulation, Pre-CFG, which incorporates CFG directly by replacing flow matching with:

$$\mathcal{L}_{\text{CFM}}^\omega = \mathbb{E} [\|F_\theta(x_t; t, t, c) - \tilde{v}_t(x_t|x)\|_2^2], \quad (20)$$

$$\tilde{v}_t(x_t|x) = F_\emptyset + \omega(v_t(x_t|x) - F_\emptyset). \quad (21)$$

We then train the flow map using the following objective:

$$\mathcal{L}_{\text{iSD-T}} = \lambda_1 \mathcal{L}_{\text{CFM}}^\omega + \lambda_2 \mathcal{L}_{\text{SD-R}} \quad (22)$$

This objective encourages the flow map to align with the ground-truth CFG velocity (see Section A.10). We refer to this case as iSD-T. We adopt iSD-T for class-conditional settings and vanilla iSD for class-unconditional settings.

6. Experiments

Experimental Settings. To evaluate our method on image generation, we conduct experiments on the ImageNet-1K (Deng et al., 2009) dataset. Following prior work, we use downsampled $32 \times 32 \times 4$ latent variables from 256×256 images encoded by a VAE (Rombach et al., 2022), and adopt a DiT (Peebles & Xie, 2023) in BF16 precision.

For unconditional settings, we validate our method on the CelebA-HQ (Karras et al., 2018) dataset, using the same latent variable settings as in the ImageNet experiments. Sample quality is measured with FID (Heusel et al., 2017) and Inception Score (IS; Salimans et al. (2016)). Further details are provided in Section C.2.

We further evaluate our method on diffusion-based policy learning to assess the applicability beyond image generation. We adopt diffusion policy benchmarks as in Chi et al. (2023), and report task success rates. These experiments are intended to examine the applicability rather than to establish new state-of-the-art results (see Section C.5 for details).

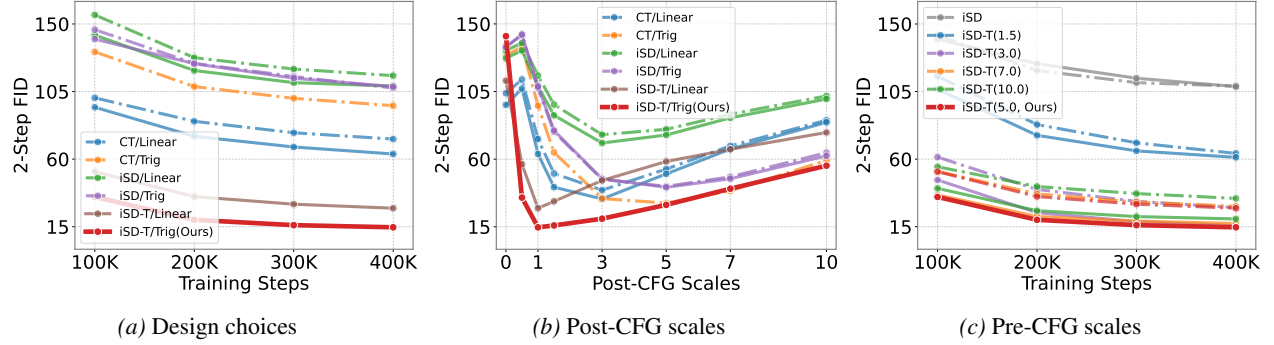


Figure 6. Design choices. (a) FIDs over training steps. Solid lines indicate the JVP approximation, and dash-dot lines indicate the exact JVP. (b) FIDs of Post-CFG over guidance scales. (c) FIDs of Pre-CFG over training steps. Solid lines indicate trigonometric interpolation, and dash-dot lines indicate linear.

Table 3. Effect of contributions on ImageNet-1K with DiT-B/4. 2-step evaluation results with standard deviations σ .

CASE	FID \downarrow ($\pm\sigma$)	IS \uparrow ($\pm\sigma$)
CONSISTENCY TRAINING	120.5 (± 3.71)	9.69 (± 0.47)
+ JOINT TRAINING w/ \mathcal{L}_{CFM}	101.3 (± 13.5)	12.70 (± 3.49)
+ RELAXING TO $s < t$	69.18 (± 2.71)	21.45 (± 1.15)
+ iSD-T ($\omega = 5.0$)	27.49 (± 0.59)	72.20 (± 2.83)
+ TRIGONOMETRIC INTERP.	15.20 (± 0.69)	181.24 (± 4.30)

Table 4. FIDs across design choices (2-Step). The numbers in the header denote Post-CFG scales.

LOSS	INTERP.	JVP	1.0	3.0	5.0	7.0
\mathcal{L}_{CT}	LINEAR	EXACT	69.18	39.50	53.38	67.70
\mathcal{L}_{iSD}	LINEAR	EXACT	116.38	76.26	79.86	89.88
\mathcal{L}_{CT}	LINEAR	APPROX	63.34	33.53	50.17	66.68
\mathcal{L}_{iSD}	LINEAR	APPROX	108.13	70.73	76.06	87.46
$\mathcal{L}_{\text{iSD-T}}$	LINEAR	APPROX	27.49	45.80	58.43	66.54
$\mathcal{L}_{\text{iSD-T}}$	TRIG.	APPROX	15.20	20.37	29.56	40.32

6.1. Ablation Study

We conduct our ablation study on ImageNet-1K using DiT-B/4. The model is trained for 400K steps, and by default, we set $\omega = 5.0$ for $\mathcal{L}_{\text{iSD-T}}$ and use conditional velocity guidance for \mathcal{L}_{CT} . All model weights are randomly initialized.

Key factors. To validate our analysis, we perform step-by-step ablation experiments aimed at improving the stability and reproducibility of consistency training, as summarized in Table 3. We measure the variance of quantitative results across five runs with different random initializations, and report mean values.

We begin with a consistency model using linear interpolation. Introducing joint training with flow matching and relaxing time improves results and reduces variance, supporting the linearization cost hypothesis. We observe that self-distillation alone converges more slowly than baseline (Table 4, Figure 6a), while incorporating Pre-CFG $\mathcal{L}_{\text{iSD-T}}$ accelerates convergence and improves performance.

Table 5. Comparison on ImageNet-1K with DiT-B/4. 2-step evaluation results with standard deviations σ under a controlled setup: the backbone, data, optimization, and training budgets are fixed, while the only difference lies in the training objective. Each method is evaluated using the CFG scale reported as optimal in its work.

CASE	FID \downarrow ($\pm\sigma$)	IS \uparrow ($\pm\sigma$)
MEANFLOW ($\omega = 3.0$)	11.48 (± 1.68)	167.60 (± 20.4)
SHORTCUT MODEL ($\omega = 1.5$)	87.52 (± 24.3)	14.94 (± 3.68)
FACM ($\omega = 1.75$)	25.52 (± 1.73)	65.42 (± 4.84)
iSD-T (OURS, $\omega = 5.0$)	15.20 (± 0.69)	181.24 (± 4.30)

Table 6. Comparison on ImageNet-1K. iSD-T uses linear interpolation with $\omega = 5.0$.

METHOD	NFE (\downarrow)	FID (\downarrow)
iCT (SONG & DHARIWAL, 2024)	2	20.3
SHORTCUT MODEL (FRANS ET AL., 2025)	1	10.6
UCGM (SUN ET AL., 2025)	1	2.10
IMM (ZHOU ET AL., 2025)	2	7.77
MEANFLOW (GENG ET AL., 2025A)	2	2.20
FACM (PENG ET AL., 2025)	2	1.32
iSD-T w/SD-VAE (OURS)	2	2.76
iSD-T w/VA-VAE (OURS)	2	2.26

Interpolation, Post-CFG. As shown in Figure 6a and Table 4, linear interpolation tends to perform better under conditional velocity guidance, whereas trigonometric one achieves a lower FID under self-distillation, particularly with Post-CFG (Figure 6b). As performance varies across settings, we leave further analysis to future work.

JVP operation. We observe that JVP approximation often yields better empirical results than exact computation, as illustrated in Figure 6a. Under BF16 precision, it tends to be more robust, as exact one is sensitive to numerical precision. The VRAM requirement of the training decreases from 25GB to 18GB on iSD-T, and the training speed improves from 1.48 steps/sec to 4.04 steps/sec on an A100 GPU.

Pre-CFG. As shown in Figure 6c and Table 4, incorporating Pre-CFG improves FIDs compared to the vanilla \mathcal{L}_{iSD} .

Table 7. Comparison on Unconditional CelebA-HQ.

MODEL	4-FID (\downarrow)	128-FID (\downarrow)
DISTILLATION-BASED METHODS		
CD (SONG ET AL., 2023)	39.6	59.5
REFLOW (LIU ET AL., 2023)	18.4	16.1
TRAINING FROM SCRATCH		
FLOW MATCHING (LIPMAN ET AL., 2023)	63.3	7.3
CT (SONG ET AL., 2023)	19.0	53.7
SHORTCUT MODEL (FRANS ET AL., 2025)	13.8	6.9
iSD (OURS)	11.3	7.1



Figure 7. 2-step results trained on ImageNet-1K with iSD-T.

It also outperforms Post-CFG, which deviates from the intended CFG field, whereas Pre-CFG aligns the flow map with the CFG velocity during training. Combining both often degrades performance, as it results in applying the guidance twice, overly skewing the trajectory.

Reproducibility. Following Table 3 and Table 5, we examine the variance of quantitative results to assess reproducibility. Compared to prior work, our setting exhibits lower variance across runs while achieving comparable performance. These results indicate that iSD-T yields more reproducible training outcomes.

6.2. Comparison with Prior Work

Unconditional Generation. We compare our method with prior approaches on CelebA-HQ 256×256 under a class-unconditional setting, using vanilla iSD without CFG. As shown in Table 7, iSD achieves comparable performance in both few-step and multi-step generation.

Conditional Generation. We further compare consistency-based approaches on ImageNet-1K under class-conditional settings, as shown in Table 5. Using DiT-B/4, iSD achieves performance comparable to prior methods while exhibiting lower variance, indicating improved reproducibility.

To examine scalability, we evaluate iSD with DiT-XL. As shown in Table 6, iSD maintains stable training behavior and comparable sample quality at this scale, without exhibiting the training instability observed in prior methods.

We note that achieving strong FID scores at this scale requires incorporating performance-oriented conditioning techniques, such as conditioning on a guidance scale or variations in latent representation. These choices are orthogonal to our analysis and are not required for stability. Importantly, applying such conditioning does not reintroduce instability, indicating that iSD provides stable training even when combined with performance-oriented augmentations.

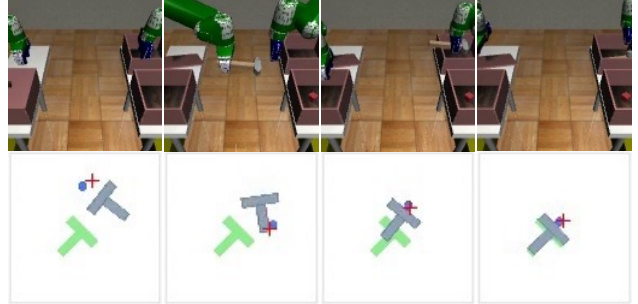


Figure 8. Simulation results of the iSD policy with NFE=2 on Transport (top) and Push-T (bottom) tasks.

 Table 8. Success rates (\uparrow) of robotic control tasks.

MODEL	NFE (\downarrow)	PUSH-T	TRANSPORT
DIFFUSION POLICY (CHI ET AL., 2023)	100 1	0.95 0.12	1.00 0.00
SHORTCUT MODEL (FRANS ET AL., 2025)	1	0.87	0.80
MEANFLOW (GENG ET AL., 2025A)	1	0.85	0.92
iSD (OURS)	2 1	0.92 0.86	1.00 0.94

ity, indicating that iSD provides stable training even when combined with performance-oriented augmentations.

6.3. Diffusion-based Policy Learning

To assess the applicability of iSD beyond image generation, we adopt it as a diffusion policy objective in robotic control tasks. Experimental settings follow prior work on diffusion-based policies (Chi et al., 2023) for transformer and state-based policy architectures.

As shown in Table 8, iSD with linear interpolation yields performance comparable to other few-step methods, under the same evaluation protocol. With 2-step sampling, iSD achieves success rates comparable to those of diffusion policies that require more sampling steps. These results indicate that iSD can serve as a stable alternative to diffusion-based objectives in policy learning.

7. Conclusion

In this work, we conducted a theoretical examination of consistency-based generative models from a flow map perspective, clarifying the sources of suboptimal convergence and training instability that limit reproducibility. This analysis explains how objective design choices influence convergence behavior in practice. Building on these insights, we revisited self-distillation and reformulated it to be compatible with consistency training, enabling more stable optimization without reliance on a pretrained diffusion model, namely a preconditioner. Finally, we demonstrated that the strategy is applicable to diffusion-based policy learning beyond image generation.

Impact Statements

This paper presents work aimed at advancing the field of machine learning by improving the theoretical understanding and training stability of consistency-based generative models. The contributions focus on analysis and objective reformulation, without introducing new model architectures, expanding model capacity, or relying on additional data.

As such, the potential ethical and societal impacts of this work are aligned with those already well established in generative modeling, including concerns related to data bias, misuse of generated content, and downstream applications. Improving training stability and reproducibility may contribute positively to research efficiency and reduce computational waste, but the work does not directly address broader societal risks, which remain important considerations for future research.

References

Albergo, M. S. and Vanden-Eijnden, E. Building normalizing flows with stochastic interpolants. In *The Eleventh International Conference on Learning Representations*, 2023.

Albergo, M. S., Boffi, N. M., and Vanden-Eijnden, E. Stochastic interpolants: A unifying framework for flows and diffusions, 2023.

Boffi, N. M., Albergo, M. S., and Vanden-Eijnden, E. How to build a consistency model: Learning flow maps via self-distillation. In *The Thirty-ninth Annual Conference on Neural Information Processing Systems*, 2025a.

Boffi, N. M., Albergo, M. S., and Vanden-Eijnden, E. Flow map matching with stochastic interpolants: A mathematical framework for consistency models. *Transactions on Machine Learning Research*, 2025b. ISSN 2835-8856.

Chi, C., Feng, S., Du, Y., Xu, Z., Cousineau, E., Burchfiel, B., and Song, S. Diffusion policy: Visuomotor policy learning via action diffusion. In *Proceedings of Robotics: Science and Systems (RSS)*, 2023.

Deng, J., Dong, W., Socher, R., Li, L.-J., Li, K., and Fei-Fei, L. Imagenet: A large-scale hierarchical image database. In *2009 IEEE Conference on Computer Vision and Pattern Recognition*, pp. 248–255, 2009. doi: 10.1109/CVPR.2009.5206848.

Esser, P., Kulal, S., Blattmann, A., Entezari, R., Müller, J., Saini, H., Levi, Y., Lorenz, D., Sauer, A., Boesel, F., Podell, D., Dockhorn, T., English, Z., and Rombach, R. Scaling rectified flow transformers for high-resolution image synthesis. In *ICML*, 2024.

Frans, K., Hafner, D., Levine, S., and Abbeel, P. One step diffusion via shortcut models. In *The Thirteenth International Conference on Learning Representations*, 2025.

Geng, Z., Deng, M., Bai, X., Kolter, J. Z., and He, K. Mean flows for one-step generative modeling. In *The Thirty-ninth Annual Conference on Neural Information Processing Systems*, 2025a.

Geng, Z., Lu, Y., Wu, Z., Shechtman, E., Kolter, J. Z., and He, K. Improved mean flows: On the challenges of fastforward generative models, 2025b.

Geng, Z., Pokle, A., Luo, W., Lin, J., and Kolter, J. Z. Consistency models made easy. In *The Thirteenth International Conference on Learning Representations*, 2025c.

Henry, A., Dachapally, P. R., Pawar, S., and Chen, Y. Query-key normalization for transformers, 2020.

Heusel, M., Ramsauer, H., Unterthiner, T., Nessler, B., and Hochreiter, S. Gans trained by a two time-scale update rule converge to a local nash equilibrium. In Guyon, I., Luxburg, U. V., Bengio, S., Wallach, H., Fergus, R., Vishwanathan, S., and Garnett, R. (eds.), *Advances in Neural Information Processing Systems*, volume 30. Curran Associates, Inc., 2017.

Ho, J. and Salimans, T. Classifier-free diffusion guidance. In *NeurIPS 2021 Workshop on Deep Generative Models and Downstream Applications*, 2021.

Ho, J., Jain, A., and Abbeel, P. Denoising diffusion probabilistic models. In Larochelle, H., Ranzato, M., Hadsell, R., Balcan, M., and Lin, H. (eds.), *Advances in Neural Information Processing Systems*, volume 33, pp. 6840–6851. Curran Associates, Inc., 2020.

Issenhuth, T., Lee, S., Santos, L. D., Franceschi, J.-Y., Kim, C., and Rakotomamonjy, A. Improving consistency models with generator-augmented flows, 2025.

Karras, T., Aila, T., Laine, S., and Lehtinen, J. Progressive growing of GANs for improved quality, stability, and variation. In *International Conference on Learning Representations*, 2018.

Kim, D., Lai, C.-H., Liao, W.-H., Murata, N., Takida, Y., Uesaka, T., He, Y., Mitsuishi, Y., and Ermon, S. Consistency trajectory models: Learning probability flow ODE trajectory of diffusion. In *The Twelfth International Conference on Learning Representations*, 2024.

Li, Z., Liu, L., Liang, C., Chen, W., and Zhao, T. Normuon: Making muon more efficient and scalable, 2025.

Lipman, Y., Chen, R. T. Q., Ben-Hamu, H., Nickel, M., and Le, M. Flow matching for generative modeling. In *The Eleventh International Conference on Learning Representations*, 2023.

Liu, X., Gong, C., and qiang liu. Flow straight and fast: Learning to generate and transfer data with rectified flow. In *The Eleventh International Conference on Learning Representations*, 2023.

Loshchilov, I. and Hutter, F. Decoupled weight decay regularization. In *International Conference on Learning Representations*, 2019.

Lu, C. and Song, Y. Simplifying, stabilizing and scaling continuous-time consistency models. In *The Thirteenth International Conference on Learning Representations*, 2025.

Peebles, W. and Xie, S. Scalable diffusion models with transformers. In *Proceedings of the IEEE/CVF International Conference on Computer Vision (ICCV)*, pp. 4195–4205, October 2023.

Peng, Y., Zhu, K., Liu, Y., Wu, P., Li, H., Sun, X., and Wu, F. Flow-anchored consistency models, 2025.

Podell, D., English, Z., Lacey, K., Blattmann, A., Dockhorn, T., Müller, J., Penna, J., and Rombach, R. SDXL: Improving latent diffusion models for high-resolution image synthesis. In *The Twelfth International Conference on Learning Representations*, 2024.

Rombach, R., Blattmann, A., Lorenz, D., Esser, P., and Ommer, B. High-resolution image synthesis with latent diffusion models. In *Proceedings of the IEEE/CVF Conference on Computer Vision and Pattern Recognition (CVPR)*, pp. 10684–10695, June 2022.

Sabour, A., Fidler, S., and Kreis, K. Align your flow: Scaling continuous-time flow map distillation, 2025.

Salimans, T. and Ho, J. Progressive distillation for fast sampling of diffusion models. In *International Conference on Learning Representations*, 2022.

Salimans, T., Goodfellow, I., Zaremba, W., Cheung, V., Radford, A., Chen, X., and Chen, X. Improved techniques for training gans. In Lee, D., Sugiyama, M., Luxburg, U., Guyon, I., and Garnett, R. (eds.), *Advances in Neural Information Processing Systems*, volume 29. Curran Associates, Inc., 2016.

Shaul, N., Singer, U., Gat, I., and Lipman, Y. Transition matching: Scalable and flexible generative modeling. In *The Thirty-ninth Annual Conference on Neural Information Processing Systems*, 2025.

Silvestri, G., Ambrogioni, L., Lai, C.-H., Takida, Y., and Mitsufuji, Y. VCT: Training consistency models with variational noise coupling. In *Forty-second International Conference on Machine Learning*, 2025.

Song, Y. and Dhariwal, P. Improved techniques for training consistency models. In *The Twelfth International Conference on Learning Representations*, 2024.

Song, Y. and Ermon, S. Generative modeling by estimating gradients of the data distribution. In Wallach, H., Larochelle, H., Beygelzimer, A., d'Alché-Buc, F., Fox, E., and Garnett, R. (eds.), *Advances in Neural Information Processing Systems*, volume 32. Curran Associates, Inc., 2019.

Song, Y. and Ermon, S. Improved techniques for training score-based generative models. In Larochelle, H., Ranzato, M., Hadsell, R., Balcan, M., and Lin, H. (eds.), *Advances in Neural Information Processing Systems*, volume 33, pp. 12438–12448. Curran Associates, Inc., 2020.

Song, Y., Sohl-Dickstein, J., Kingma, D. P., Kumar, A., Ermon, S., and Poole, B. Score-based generative modeling through stochastic differential equations. In *International Conference on Learning Representations*, 2021.

Song, Y., Dhariwal, P., Chen, M., and Sutskever, I. Consistency models. In Krause, A., Brunskill, E., Cho, K., Engelhardt, B., Sabato, S., and Scarlett, J. (eds.), *Proceedings of the 40th International Conference on Machine Learning*, volume 202 of *Proceedings of Machine Learning Research*, pp. 32211–32252. PMLR, 23–29 Jul 2023.

Su, J., Lu, Y., Pan, S., Murtadha, A., Wen, B., and Liu, Y. Roformer: Enhanced transformer with rotary position embedding, 2023.

Sun, P., Jiang, Y., and Lin, T. Unified continuous generative models. *arXiv preprint arXiv:2505.07447*, 2025.

Xiao, Z., Kreis, K., and Vahdat, A. Tackling the generative learning trilemma with denoising diffusion GANs. In *International Conference on Learning Representations*, 2022.

Yang, L., Zhang, Z., Zhang, Z., Liu, X., Xu, M., Zhang, W., Meng, C., Ermon, S., and Cui, B. Consistency flow matching: Defining straight flows with velocity consistency, 2024.

Yao, J., Yang, B., and Wang, X. Reconstruction vs. generation: Taming optimization dilemma in latent diffusion models. In *Proceedings of the IEEE/CVF Conference on Computer Vision and Pattern Recognition*, 2025.

Yao, Z., Gholami, A., Keutzer, K., and Mahoney, M. Pyhessian: Neural networks through the lens of the hessian. In *ICML workshop on Beyond First-Order Optimization Methods in Machine Learning*, 2020.

Yin, T., Gharbi, M., Park, T., Zhang, R., Shechtman, E., Durand, F., and Freeman, W. T. Improved distribution matching distillation for fast image synthesis. In *The Thirty-eighth Annual Conference on Neural Information Processing Systems*, 2024a.

Yin, T., Gharbi, M., Zhang, R., Shechtman, E., Durand, F., Freeman, W. T., and Park, T. One-step diffusion with distribution matching distillation. In *Proceedings of the IEEE/CVF Conference on Computer Vision and Pattern Recognition*, 2024b.

Zhang, B. and Sennrich, R. Root mean square layer normalization. In Wallach, H., Larochelle, H., Beygelzimer, A., d'Alché-Buc, F., Fox, E., and Garnett, R. (eds.), *Advances in Neural Information Processing Systems*, volume 32. Curran Associates, Inc., 2019.

Zhou, L., Ermon, S., and Song, J. Inductive moment matching. In *Forty-second International Conference on Machine Learning*, 2025.

Zhou, M., Zheng, H., Wang, Z., Yin, M., and Huang, H. Score identity distillation: Exponentially fast distillation of pretrained diffusion models for one-step generation. In *Forty-first International Conference on Machine Learning*, 2024.

A. Theoretical Analysis of Flow Map Models

A.1. Mean collapse of Diffusion and Flow Matching Models

Posterior Distribution. First, consider the data distribution $p_X(x) = \mathcal{N}(\mu_X, \sigma_X^2)$ and the interpolation $x_t = \alpha_t x + \sigma_t z$. The conditional distribution is given by $p(x_t = y|x) = \mathcal{N}(y; \alpha_t x, \sigma_t^2)$. By Bayes' rule,

$$\begin{aligned} p(x|x_t = y) &\propto p(x_t = y|x)p(x) \\ &= \mathcal{N}(y; \alpha_t x, \sigma_t^2)\mathcal{N}(x; \mu_X, \sigma_X^2) \\ &\propto \exp\left(-\frac{(y - \alpha_t x)^2}{2\sigma_t^2} - \frac{(x - \mu_X)^2}{2\sigma_X^2}\right) \\ &= \exp\left(\left(\frac{1}{2\sigma_X^2} + \frac{\alpha_t^2}{2\sigma_t^2}\right)x^2 - \left(\frac{\mu_X}{\sigma_X^2} + \frac{\alpha_t y}{\sigma_t^2}\right)x + \left(\frac{\mu^2}{2\sigma_X^2} + \frac{y^2}{2\sigma_t^2}\right)\right). \end{aligned}$$

This can be organized as a Gaussian with a closed form $p(x|x_t = y) = \mathcal{N}(\mu_{x|y,t}, \sigma_{x|y,t}^2)$ where

$$\mu_{x|y,t} = \frac{\alpha_t \sigma_X^2 y + \mu_X \sigma_t^2}{\sigma_t^2 + \sigma_X^2 \alpha_t^2}, \quad \sigma_{x|s,t}^2 = \frac{\sigma_X^2 \sigma_t^2}{\sigma_t^2 + \sigma_X^2 \alpha_t^2}.$$

Extending the data distribution to a mixture of Gaussians $p_X(x) = \sum_i \pi_i \mathcal{N}(x; \mu_i, \sigma_i^2)$, we introduce the latent variable π for handling π_i :

$$p(\pi = i) = \pi_i, \quad p(x|\pi = i) = \mathcal{N}(x; \mu_i, \sigma_i^2).$$

Then, the marginal distribution $p(x_t = y|\pi = i)$ can be expressed as

$$\begin{aligned} p(x_t = y|\pi = i) &= \int p(x_t = y|x)p(x|\pi = i)dx \\ &= \int \mathcal{N}(y; \alpha_t x, \sigma_t^2)\mathcal{N}(x; \mu_i, \sigma_i^2)dx \\ &= \mathcal{N}(y; \alpha_t \mu_i, \alpha_t^2 \sigma_i^2 + \sigma_t^2). \end{aligned}$$

And we define responsibilities $r_i(y)$ as posterior distribution

$$r_{i,t}(y) = p(\pi = i|x_t = y) = \frac{p(x_t = y|\pi = i)p(\pi = i)}{\sum_j p(x_t = y|\pi = j)p(\pi = j)} = \frac{\pi_i \mathcal{N}(y; \alpha_t \mu_i, \alpha_t^2 \sigma_i^2 + \sigma_t^2)}{\sum_j \pi_j \mathcal{N}(y; \alpha_t \mu_j, \alpha_t^2 \sigma_j^2 + \sigma_t^2)}.$$

Therefore, the posterior distribution $p(x|x_t = y)$ is

$$\begin{aligned} p(x|x_t = y) &= \sum_i p(\pi = i|x_t = y)p(x|x_t = y, \pi = i) \\ &= \sum_i r_{i,t}(y) \mathcal{N}(y; \alpha_t x, \sigma_t^2) \mathcal{N}(x; \mu_i, \sigma_i^2) \\ &= \sum_i r_{i,t}(y) \mathcal{N}(x; \mu_{x|i,y,t}, \sigma_{x|i,y,t}^2) \\ \text{where } \mu_{x|i,y,t} &= \frac{\alpha_t \sigma_i^2 y + \mu_i \sigma_t^2}{\sigma_t^2 + \sigma_i^2 \alpha_t^2}, \quad \sigma_{x|i,y,t}^2 = \frac{\sigma_i^2 \sigma_t^2}{\sigma_t^2 + \sigma_i^2 \alpha_t^2}. \end{aligned}$$

Particularly, we observe that $\mu_{x|i,y,1} = \mu_i$, $\sigma_{x|i,y,1}^2 = \sigma_i^2$ and $r_{i,1}(y) = \pi_i$.

One-step Generation. Under the linear trajectory $x_t = (1-t)x + tz$, the conditional velocity is $v_t(x_t|x) = z - x$. Thus, one-step generation is defined by

$$\begin{aligned} f_F(x_t; t) &= x_t - tF^*(x_t; t) = x_t - t \mathbb{E}_{x|x_t} [v_t(x_t|x)] \\ &= \mathbb{E}_{x,z|x_t} [x_t - t(z - x)] \\ &= \mathbb{E}_{x|x_t} [x]. \end{aligned}$$

In the unimodal Gaussian case, $\mathbb{E}_{x|z}[x] = \mu_{x|z,1} = \mu_X$ and the one-step generated samples collapse to the mean of the data distribution. Similarly, in the mixture of Gaussians case, one-step generated samples collapse to the mixture mean.

$$f_F(z) = \mathbb{E}_{x|z}[x] = \sum_i r_i(z) \mu_{i|z,1} = \sum_i \pi_i \mu_i = \mu_X.$$

Thus, one-step generation collapses to the data mean μ_X regardless of the input. \square

A.2. Injectivity of Flow Map

Since the marginal velocity is assumed to be Lipschitz continuous, the Picard-Lindelöf theorem guarantees a unique solution to the ODE $dx_t = v_t^*(x_t)dt$ for any initial value. The non-crossing trajectory follows directly, since any crossing would contradict uniqueness. Thus, since the flow map is formulated as the solution of the ODE with the initial value x_t , it is well-defined, and the solution x_s is uniquely determined by non-crossing, ensuring the injectivity of the flow map.

A.3. Eulerian Equation and Uniqueness of Flow Map

Suppose the ground-truth flow map is defined as

$$f_{t,s}^*(x_t) = x_t + \int_t^s v_\tau^*(x_\tau) d\tau = x_s.$$

By construction, the identity mapping $f_{t,s}^*(f_{s,t}^*(x_s)) = x_s$ satisfies. Differentiating both sides w.r.t. t yields

$$\frac{d}{dt} f_{t,s}^*(f_{s,t}^*(x_s)) = \partial_t f_{t,s}^*(f_{s,t}^*(x_s)) + \partial_t f_{s,t}^*(x_s) \cdot \nabla_x f_{t,s}^*(f_{s,t}^*(x_s)) = \frac{d}{dt} x_s = 0.$$

Using $f_{s,t}^*(x_s) = x_t$ and $\partial_t f_{s,t}^*(x_s) = \partial_t x_t = v_t^*(x_t)$, we obtain the Eulerian equation:

$$\frac{d}{dt} f_{t,s}^*(x_t) = \partial_t f_{t,s}^*(x_t) + v_t^*(x_t) \cdot \nabla_x f_{t,s}^*(x_t) = 0.$$

Suppose a trainable network $f_\theta(x; t, s) = f_{t,s}^\theta(x)$ is continuous in x, t, s , Lipschitz continuous in x , and satisfies the boundary condition $f_{s,s}^\theta(x) = x$ for all s . If f_θ satisfies the Eulerian equation, $f_{t,s}^\theta$ remains constant along the characteristic curve induced by $v_t^*(x_t)$.

Let χ_τ denotes the characteristic curve defined on $[s, t]$ by $\chi_t = x$ and $\chi'_\tau = v_\tau^*(\chi_\tau)$. Along this curve, $f_{\tau,s}^\theta$ is constant and evaluating at $\tau = t$ and $\tau = s$ yields

$$f_{t,s}^\theta(x) = f_{t,s}^\theta(\chi_t) = f_{s,s}^\theta(\chi_s) = \chi_s = f_{t,s}^*(x),$$

since $f_{t,s}^*$ generates the characteristic curve χ_τ by its definition. Thus, the learned mapping coincides with the exact flow map. \square

A.4. Interpolation condition

We begin by explicitly deriving the solution of the Eulerian equation. For $f_{t,s}^\theta(x_t) = \nu_t^{-1}(A'_{t,s}x_t - A_{t,s}F_{t,s}^\theta(x_t))$ in Equation (7), let $n = A'_{t,s}x_t - A_{t,s}F_{t,s}^\theta(x_t)$, which simplifies to $n = A'x_t - AF$ and $f = \nu_t^{-1}n$. Then, differentiation with respect to timestep t yields

$$\begin{aligned} n' &= A''x_t + A'(v_t - F) - AF', \\ f' &= [A''x_t + A'(v_t - F) - AF']\frac{\nu_t}{\nu_t^2} + [A'x_t - AF]\frac{\nu'_t}{\nu_t^2}. \end{aligned}$$

Assuming $f' = 0$ and $\nu_t \neq 0$, we obtain

$$A\nu_t F' = -(A'\nu_t + A\nu'_t)F + [A''\nu_t x_t + A'\nu_t v_t + A'\nu'_t x_t],$$

which further simplifies to

$$A\nu_t F' = -[A\nu_t]' F + [A\nu_t x_t]' = BF' = -B'F + D',$$

where $B = A\nu_t$, $D = A'\nu_t x_t$. Since $BF' + B'F = [BF]'$, we obtain $[BF]' = D'$, which yields $A\nu_t F = A'\nu_t x_t + C$ for some integration constant C . Assuming $A = A_{t,s} = \alpha_s \sigma_t - \sigma_s \alpha_t \neq 0$ for $t \neq s$, this gives $F = A'A^{-1}x_t + C(A\nu_t)^{-1}$, and hence

$$f_{t,s}^*(x_t) = \nu_t^{-1}[A'x_t - A'\nu_t x_t - C\nu_t^{-1}] = -C\nu_t^{-2}.$$

If ν_t is a time-dependent scalar, the global optimum $f^* = -C'\nu_t^{-2}$ is itself time-dependent, so the Eulerian equation can't vanish. If $C = 0$, the solution collapses to the trivial case $f_{t,s}^*(x_t) = 0$. Therefore, ν_t must be a time-independent constant. \square

Additional Observation. Suppose that the monotonically increasing γ_t over $t \in [0, 1]$ satisfying the boundary conditions $\gamma_1 = 1$ and $\gamma_0 = 0$. Consider the interpolation defined by $\alpha_t = (1 - \gamma_t)^c$ and $\sigma_t = \gamma_t^c$ for some constant $c \in [0.5, 1]$. Then, ν_t can be written as $\nu_t = c(1 - \gamma_t)^{c-1}\gamma_t^{c-1}\gamma_t'$. Imposing $\nu_t = \nu$ gives $\gamma_t' = \nu[c(1 - \gamma_t)^{c-1}\gamma_t^{c-1}]^{-1}$ and $c(1 - \gamma)^{c-1}\gamma^{c-1}d\gamma = \nu dt$. Integrating both sides yields

$$c \int (1 - \gamma)^{c-1}\gamma^{c-1}d\gamma = \nu \int dt = \nu(t + C),$$

where the constant C vanishes due to $\gamma_0 = 0$. For the incomplete beta function B , this becomes

$$cB(\gamma_t; c, c) = c \int_0^{\gamma_t} (1 - \eta)^{c-1}\eta^{c-1}d\eta = \nu \int_0^t d\tau = \nu t.$$

By the boundary condition, $cB(c, c) = cB(1; c, c) = \nu$, and thus γ_t is characterized by

$$cB(\gamma_t; c, c) = \nu \frac{cB(\gamma_t; c, c)}{cB(c, c)} = \nu I_{\gamma_t}(c, c) = \nu t \implies \gamma_t = I_t^{-1}(c, c),$$

where I denotes the regularized incomplete beta function.

In this case, γ_t is characterized regardless of ν . Particularly, when $c = 0.5$, we obtain $\gamma_t = \sin^2(\frac{\pi}{2}t)$, which yields trigonometric interpolation $\alpha_t = \cos(\frac{\pi}{2}t)$ and $\sigma_t = \sin(\frac{\pi}{2}t)$. On the other hand, when $c = 1$, we have $\gamma_t = t$, $\alpha_t = 1 - t$, $\sigma_t = t$, and which reduces to linear interpolation. Interpolating c between 0.5 and 1.0 is a promising approach for formulating the consistency model.

A.5. Recent Consistency-based Generative Models are Flow Map Models

sCT. Under trigonometric interpolation $x_t = \cos(t)x + \sin(t)z$,

$$f_\theta(x_t; t, s) = \cos(s - t)x_t + \sin(s - t)F_\theta(x_t; t, s).$$

When $s = 0$

$$f_\theta(x_t; t) = \cos(t)x_t - \sin(t)F_\theta(x_t; t),$$

which exactly recovers the sCT formulation. If consistency training is formulated without the stop-gradient operation, then the objective reduces to the direct training objective as $\Delta t \rightarrow 0$.

$$\begin{aligned} & \mathbb{E} \left[\|f_\theta(x_t; t, s) - f_\theta(x_{t-\Delta t}; t - \Delta t, s)\|_2^2 \right] \\ &= \mathbb{E} \left[\|f_\theta(x_t; t, s) - [f_\theta(x_t; t, s) - \partial_t f_\theta(x_t; t, s) \cdot \Delta t - \nabla_x f_\theta(x_t; t, s) \cdot v(x_t | x) \cdot \Delta t + O(\Delta t^2)]\|_2^2 \right] \\ &= \Delta t^2 \cdot \mathbb{E} \left[\|\partial_t f_\theta(x_t; t, s) + v(x_t | x) \cdot \nabla_x f_\theta(x_t; t, s)\|_2^2 \right] + O(\Delta t^3). \end{aligned}$$

However, if we utilize the stop-gradient, the continuous-time consistency training objective is defined as

$$\begin{aligned}
 & \nabla_{\theta} \mathbb{E} \left[\|f_{\theta}(x_t; t, s) - f_{\theta^-}(x_{t-\Delta t}; t - \Delta t, s)\|_2^2 \right] \\
 &= \mathbb{E} [2 \nabla_{\theta} f_{\theta}(x_t; t, s) \cdot (f_{\theta^-}(x_t; t, s) - f_{\theta^-}(x_{t-\Delta t}; t - \Delta t, s))] \\
 &= 2 \Delta t \cdot \nabla_{\theta} \mathbb{E} \left[f_{\theta}(x_t; t, s) \cdot \frac{f_{\theta^-}(x_t; t, s) - f_{\theta^-}(x_{t-\Delta t}; t - \Delta t, s)}{\Delta t} \right] \\
 \implies \mathcal{L}_{\text{CT}} &= \mathbb{E} \left[f_{\theta}(x_t; t, s) \frac{df_{\theta^-}(x_t; t, s)}{dt} \right].
 \end{aligned}$$

By the mean value theorem,

$$f_{\theta^-}(x_t; t, s) = f_{\theta}(x_t; t, s) + \nabla_{\theta} f_{\zeta}(x_t; t, s) \cdot (\theta^- - \theta),$$

for the parameter ζ lying between θ and θ^- . Using this, we can show that

$$\begin{aligned}
 & \mathbb{E} \left[\|f_{\theta}(x_t; t, s) - f_{\theta^-}(x_t; \hat{t}, s)\|_2^2 \right] \\
 &= \mathbb{E} \left[\|f_{\theta}(x_t; t, s) - f_{\theta}(x_{\hat{t}}; \hat{t}, s) - \nabla_{\theta} f_{\zeta}(x_{\hat{t}}; \hat{t}, s) \cdot (\theta^- - \theta)\|_2^2 \right] \\
 &= \mathbb{E} \left[\|\partial_t f_{\theta}(x_t; t, s) \cdot \Delta t + \nabla_x f_{\theta}(x_t; t, s) \cdot v(x_t | x) \cdot \Delta t - \nabla_{\theta} f_{\zeta}(x_{\hat{t}}; \hat{t}, s) \cdot (\theta^- - \theta) + O(\Delta t^2)\|_2^2 \right] \\
 &= \mathcal{L}_{\text{DT}} \cdot \Delta t^2 - 2 \mathbb{E} \left[L f_{\theta}(x_t; t, s) \cdot J_{\hat{t}, s}^{\zeta} \cdot \Delta \theta \right] \cdot \Delta t + \mathbb{E} \left[\|J_{\hat{t}, s}^{\zeta} \cdot \Delta \theta\|_2^2 \right] + O(\Delta t^3) + O(\Delta t^2 \|\Delta \theta\|),
 \end{aligned}$$

where $\hat{t} = t - \Delta t$, $\Delta \theta = \theta^- - \theta$, $J_{\hat{t}, s}^{\zeta} = \nabla_{\theta} f_{\zeta}(x_{\hat{t}}; \hat{t}, s)$, and the operator is defined as $L f = \partial_t f + v \cdot \nabla_x f$. In this case, since f is Lipschitz and has a bounded first derivative, $L f$ and J are bounded. Hence, $2(L f \cdot \Delta t - J \cdot \Delta \theta) \cdot O(\Delta t^2) = O(\Delta t^3) + O(\Delta t^2 \|\Delta \theta\|)$. If we set $\theta^- = \text{sg}[\theta]$, this reduces to

$$\mathbb{E} \left[\|f_{\theta}(x_t; t, s) - f_{\theta^-}(x_{t-\Delta t}; t - \Delta t, s)\|_2^2 \right] = \mathcal{L}_{\text{DT}} \cdot \Delta t^2 + O(\Delta t^3).$$

Thus, the formulation can be interpreted as the direct training objective.

From another perspective, since the time derivative of $f_{t,s}^{\theta}(x_t) = f_{\theta}(x_t; t, s)$ is given by

$$\frac{df_{t,s}^{\theta}(x_t)}{dt} = \partial_t f_{t,s}^{\theta}(x_t) + v(x_t | x) \cdot \nabla_x f_{t,s}^{\theta}(x_t) = (L_* f_{t,s}^{\theta})(x_t) + \Delta v \cdot \nabla_x f_{t,s}^{\theta}(x_t),$$

where $\Delta v = v_t(x_t | x) - v_t^*(x_t)$ and $L_* f_{t,s} = \partial_t f_{t,s} + v_t^* \cdot \nabla_x f_{t,s}$, the objective can be written as

$$\mathcal{L}_{\text{CT}} = \mathbb{E} \left[f_{t,s}^{\theta} \left(L_* f_{t,s}^{\theta^-} \right) + f_{t,s}^{\theta} \left(\Delta v \cdot \nabla_x f_{t,s}^{\theta^-} \right) \right].$$

The first term on the right-hand side corresponds to Eulerian distillation. By the tower property, the second term vanishes under conditional expectation:

$$\begin{aligned}
 \mathbb{E}_{x,z,t,s} \left[f_{t,s}^{\theta} (\Delta v \cdot \nabla_x f_{t,s}^{\theta^-}) \right] &= \mathbb{E}_{x,z,t,s} \left[\mathbb{E}_{\tilde{x}|x_t} \left[f_{t,s}^{\theta} (\Delta v \cdot \nabla_x f_{t,s}^{\theta^-}) \right] \right] \\
 &= \mathbb{E}_{x,z,t,s} \left[f_{t,s}^{\theta} \left(\mathbb{E}_{\tilde{x}|x_t} [\Delta v] \cdot \nabla_x f_{t,s}^{\theta^-} \right) \right] \\
 &= \mathbb{E}_{x,z,t,s} \left[f_{t,s}^{\theta} \cdot 0 \cdot \nabla_x f_{t,s}^{\theta^-} \right] = 0.
 \end{aligned}$$

Thus, \mathcal{L}_{CT} reduces in value to Eulerian distillation even along the conditional trajectory. However, the gradients of Eulerian distillation and consistency training differ, and their training dynamics may therefore exhibit distinct behaviors. The instability of these gradient dynamics is discussed in Section A.7. \square

MeanFlow. Suppose a flow map model under linear interpolation.

$$f_{\theta}(x_t; t, s) = x_t + (s - t)F_{\theta}(x_t; t, s), \quad x_t = (1 - t)x + tz.$$

The corresponding direct training objective is

$$\mathcal{L}(\theta) = \mathbb{E} \left[\left\| \partial_t f_{t,s}^\theta(x_t) + v(x_t|x) \cdot \nabla_x f_{t,s}^\theta(x_t) \right\|_2^2 \right] = \mathbb{E} \left[\left\| \frac{df_{t,s}^\theta(x_t)}{dt} \right\|_2^2 \right],$$

where

$$\frac{d}{dt} f_\theta(x_t; t, s) = v_t - F_\theta(x_t; t, s) + (s - t) \frac{d}{dt} F_\theta(x_t; t, s).$$

Recall the MeanFlow objective from (Geng et al., 2025a)

$$\mathcal{L}(\theta) = \mathbb{E}[\|u_\theta(z_t; r, t) - \text{sg}[v_t - (t - r)(v_t \cdot \partial_z u_\theta + \partial_t u_\theta)]\|_2^2].$$

Rewrite the MeanFlow objective by using flow map notation and transform

$$\begin{aligned} & \nabla_\theta \mathbb{E} [\|F_\theta(x_t; t, s) - \text{sg}[v_t(x_t|x) - (t - s)(v_t(x_t|x) \cdot \nabla_x F_\theta + \partial_t F_\theta)]\|_2^2] \\ &= \nabla_\theta \mathbb{E} \left[\left\| v_t(x_t|x) - F_\theta(x_t; t, s) + (s - t) \cdot \frac{d}{dt} F_\theta(x_t; t, s) \right\|_2^2 \right] \\ &= \nabla_\theta \mathbb{E} \left[\left\| F_\theta(x_t; t, s) - F_{\theta-}(x_t; t, s) - \left[v_t(x_t|x) - F_{\theta-}(x_t; t, s) + (s - t) \frac{d}{dt} F_{\theta-}(x_t; t, s) \right] \right\|_2^2 \right] \\ &= \nabla_\theta \mathbb{E} \left[\frac{1}{t - s} f_\theta(x_t; t, s) \frac{df_{\theta-}(x_t; t, s)}{dt} \right]. \end{aligned}$$

Thus, the MeanFlow objective is a special case of the continuous-time consistency training with conditional velocity under linear interpolation. \square

Shortcut Model. From (Frans et al., 2025), the Shortcut Model objective consists of the flow matching objective and the consistency objective.

$$\mathcal{L}_{\text{SC}} = \mathbb{E}[\|s_\theta(x_t; t, 0) - v_t\|_2^2 + \|s_\theta(x_t; t, 2d) - [s_\theta(x_t; t, d) + s_\theta(x'_{t+d}; t + d, d)]/2\|_2^2],$$

with $x'_{t+d} = x_t + s_\theta(x_t, t, d)$. By setting $d = s - t$ and $F_\theta(x_t; t, s) = s_\theta(x_t; t, s - t)$, sampling $t \sim \mathcal{U}[0, 1]$, and choosing $s = t - 2^{-d'}$ for $d' \sim \text{Cat}[1, 7]$, we obtain the flow map under linear interpolation

$$f_\theta(x_t; t, s) = x_t + (s - t)F_\theta(x_t; t, s) = x'_{t+d}.$$

We can rewrite the flow matching objective of the Shortcut model as

$$\|s_\theta(x_t; t, 0) - v_t\|_2^2 = \|F_\theta(x_t; t, t) - v_t(x_t|x)\|_2^2.$$

For $r = s + d$, the consistency objective of the Shortcut Model can be written in the form of the semigroup condition, $f_{t,r}(x_t) = f_{s,r}(f_{t,s}(x_t))$:

$$\begin{aligned} & \|s_\theta(x_t; t, 2d) - [s_\theta(x_t; t, d) + s_\theta(x'_{t+d}; t + d, d)]/2\|_2^2 \\ &= \|F_\theta(x_t; t, r) - [F_\theta(x_t; t, s) + F_\theta(f_\theta(x_t; t, s); s, r)]/2\|_2^2 \\ &= \frac{1}{4d^2} \|x_t + 2d \cdot F_\theta(x_t; t, r) - x_t - 2d[F_\theta(x_t; t, s) + F_\theta(f_\theta(x_t; t, s); s, r)]/2\|_2^2 \\ &= \frac{1}{4d^2} \|x_t + 2d \cdot F_\theta(x_t; t, r) - [x_t + d \cdot F_\theta(x_t; t, s) + d \cdot F_\theta(f_\theta(x_t; t, s); s, r)]\|_2^2 \\ &= \frac{1}{4d^2} \|f_\theta(x_t; t, r) - [f_\theta(x_t; t, s) + d \cdot F_\theta(f_\theta(x_t; t, s); s, r)]\|_2^2 \\ &= \frac{1}{4d^2} \|f_\theta(x_t; t, r) - f_\theta(f_\theta(x_t; t, s); s, r)\|_2^2. \end{aligned}$$

Hence, the objective of the Shortcut Model is

$$\mathcal{L}(\theta) = \mathbb{E} \left[\|F_\theta(x_t; t, t) - v_t\|_2^2 + \frac{1}{4d^2} \|f_\theta(x_t; t, r) - f_\theta(f_\theta(x_t; t, s); s, r)\|_2^2 \right].$$

With the Taylor approximation of $F_{t,s} = F_{t,s}(x_t) = F_\theta(x_t; t, s)$

$$F_{t,r} = F_{t,s} + d \cdot \partial_s F_{t,s} + O(d^2), \quad F_{s,r} = F_{t,s} + d \cdot \partial_t F_{t,s} + d \cdot \partial_s F_{t,s} + d \cdot F_{t,s}^T \nabla_x F_{t,s} + O(d^2),$$

we obtain

$$\begin{aligned} & d[2F_{t,r} - F_{t,s} - F_{s,r}] \\ &= d[2[F_{t,s} + d \cdot \partial_s F_{t,s}] - F_{t,s} - [F_{t,s} + d \cdot \partial_t F_{t,s} + d \cdot \partial_s F_{t,s} + d \cdot F_{t,s}^T \nabla_x F_{t,s}]] + O(d^3) \\ &= d^2[\partial_s F_{t,s} - \partial_t F_{t,s} - F_{t,s}^T \nabla_x F_{t,s}] + O(d^3). \end{aligned}$$

Thus,

$$\frac{1}{4d^2} \|f_{t,r}(x_t) - f_{s,r}(f_{t,s}(x_t))\|_2^2 = \frac{d^2}{4} \|\partial_s F_{t,s} - \partial_t F_{t,s} - F_{t,s}^T \nabla_x F_{t,s}\|_2^2 + O(d^3).$$

The differentiation of the linear flow map with respect to timestep t is given by

$$f'_{t,s}(x_t) = v_t^* - F_{t,s}(x_t) + (s - t) \cdot (\partial_t F_{t,s} + v_t^* \cdot \nabla_x F_{t,s}).$$

With the Taylor approximation and the relation $F_{t,t} \approx v_t^*$ obtained from \mathcal{L}_{CFM} , we have

$$F_{t,s} = F_{t,t} + d \cdot \partial_s F_{t,t} + O(d^2) \approx v_t^* + d \cdot \partial_s F_{t,t} + O(d^2).$$

The identity $\partial_s F_{t,s} = \partial_s F_{t,t} + O(d)$ implies

$$v_t^* - F_{t,s}(x_t) = -d \cdot \partial_s F_{t,t} + O(d^2).$$

Hence,

$$f'(x_t) = d[\partial_t F_{t,s} + v_t^* \cdot \nabla_x F_{t,s} - \partial_s F_{t,s}] + O(d^2).$$

Since $v_t^* \approx F_{t,t} = F_{t,s} + O(d)$, we further obtain

$$\begin{aligned} f'(x_t) &= d[\partial_t F_{t,s} + F_{t,s} \cdot \nabla_x F_{t,s} - \partial_s F_{t,s}] + O(d^2) \\ \implies \mathcal{L} &= \mathbb{E}_{x,z,t,s} \left[\|F_\theta(x_t; t, t) - v_t\|_2^2 + \frac{1}{4} \left\| \frac{d}{dt} f_\theta(x_t; t, s) \right\|_2^2 + O(d^3) \right]. \end{aligned}$$

We observe that there is a discrepancy between Eulerian distillation, $\|v_t^* - F_{t,s} + d(\partial_t F_{t,s} + v_t^* \cdot \nabla_x F_{t,s})\|_2^2$. The first v_t^* term corresponds to $F_{t,t}$, while the second v_t corresponds to $F_{t,s}$. Alternatively, since $F_{t,t} = F_{t,s} + O(d)$, both terms can be represented in terms of $F_{t,t}$.

In the case of $F_{t,t}$, the model learns $F_{t,t}^\theta(x_t) \approx v_t^*(x_t)$ due to the loss term of $\|F_{t,t}^\theta(x_t) - v_t(x_t)\|_2^2$. This can be interpreted as the model learning a flow map corresponding to the trajectory induced by an approximated marginal velocity. Therefore, the Shortcut Model can be seen as Eulerian self-distillation under an $O((t-s)^3)$ bound. \square

Consistency Trajectory Model. Consistency Trajectory Model (CTM) trains a network to satisfy the semigroup condition of flow map, $f_{t,r}(x_t) = f_{t,s}(f_{s,r}(x_t))$, using the following objective:

$$\mathcal{L}_{\text{CTM}} = \mathbb{E}[\|f_{\theta-}(f_\theta(x_t; t, r); r, 0) - f_{\theta-}(f_{\theta-}(\Phi(x_t; t, s); s, r); r, 0)\|_2^2],$$

where Φ denotes a flow map along the learned flow of the teacher network, and timesteps satisfy $0 < r < s < t$. They show that it converges to the teacher flow map, in the version without the stop-gradient operation:

$$\mathcal{L}_{\text{CTM}} = \mathbb{E}[\|f_\theta(f_\theta(x_t; t, r); r, 0) - f_\theta(f_\theta(\Phi(x_t; t, s); s, r); r, 0)\|_2^2].$$

In the flow map perspective, while they assume a variance-exploding process and an x -prediction network in this setting, their velocity model follows the same formulation as linear flow (i.e., $v_t(x_t|x) = t^{-1}(x_t - x)$), and the flow map formulation is also consistent with it. Therefore, for analytical convenience, we adopt a linear interpolation-based formulation.

As shown in relation to the shortcut model, the semigroup-based objective, $\|f_\theta(x_t; t, r) - f_\theta(f_\theta(x_t; t, s); s, r)\|_2^2$, can be interpreted as a weighted Eulerian self-distillation framework. In addition, Boffi et al. (2025a) proves that the semigroup-based objective, denoted as progressive self-distillation, encourages the network to learn the desired flow map.

Since CTM aims to distill the knowledge of the teacher velocity network, it replaces the inner flow map $f_\theta(x_t; t, s)$ with the teacher network $\Phi(x_t; t, s)$. If we assume that CTM uses the metric function of $d_r(x, y) = \|f_{\theta-}(x; r, 0) - f_{\theta-}(y; r, 0)\|_2^2$, this objective reduces to $d(f_\theta(x_t; t, r), f_{\theta-}(\Phi(x_t; t, s); s, r))$ and we can view it as an a semigroup-based flow map model, which can be interpreted as an Eulerian distillation under an asymptotic gap. \square

Consistency Flow Matching. For linear interpolation $x_t = (1 - t)x + tz$, define

$$f_\theta(x_t; t, s = 0) = x_t - tF_\theta(x_t; t, s = 0) \implies f_\theta(x_t; t) = x_t - tF_\theta(x_t; t).$$

Then, the Consistency Flow Matching objective from (Yang et al., 2024) becomes

$$\mathcal{L}(\theta) = \mathbb{E} [\|f_\theta(x_t; t) - f_{\theta-}(x_{t-\Delta t}; t - \Delta t)\|_2^2 + \alpha \|F_\theta(x_t; t) - F_{\theta-}(x_{t-\Delta t}; t - \Delta t)\|_2^2].$$

The first term on the right side is the Taylor approximation of the consistency training objective, and the second term is the regularizer. Hence, we interpret Consistency Flow Matching as a training flow map model via the approximation with regularization. \square

UCGM. For arbitrary interpolation of α_t, σ_t , setting $s = 0$ yields

$$f_\theta(x_t; t) = \nu_t^{-1}(\sigma_t' x_t - \sigma_t F_\theta).$$

We can reformulate the objective while keeping the gradient unchanged:

$$\begin{aligned} & \nabla_\theta \|f_\theta(x_t; t) - f_{\theta-}(x_{\lambda t}; \lambda t)\|_2^2 \\ &= 2[\nabla_\theta f_\theta(x_t; t)]^T (t - \lambda t) \frac{f_{\theta-}(x_t; t) - f_{\theta-}(x_{\lambda t}; \lambda t)}{t - \lambda t} \\ & \propto [\nabla_\theta f_\theta(x_t; t)]^T \frac{f_{\theta-}(x_t; t) - f_{\theta-}(x_{\lambda t}; \lambda t)}{t - \lambda t} \\ &= \frac{\sigma_t}{\nu_t} [\nabla_\theta F_\theta(x_t; t)]^T \frac{f_{\theta-}(x_t; t) - f_{\theta-}(x_{\lambda t}; \lambda t)}{t - \lambda t} \\ &= \nabla_\theta \left\| F_\theta(x_t; t) - F_{\theta-}(x_t; t) + \frac{\sigma_t [f_{\theta-}(x_t; t) - f_{\theta-}(x_{\lambda t}; \lambda t)]}{\nu_t (t - \lambda t)} \right\|_2^2, \end{aligned}$$

which is identical to the objective of UCGM. When $\lambda = 0$, this reduces to the flow matching objective since $\lambda t = 0$ collapses $f_{\theta-}(x_0; 0) = x_0$. In this case, the objective becomes origin prediction, which in turn yields F_θ with a velocity-matching objective. Otherwise, setting $\lambda \rightarrow 1$ reduces the objective to consistency training by $\Delta = F_\theta(x_t; t) - F_{\theta-}(x_t; t) + \frac{\sigma_t}{\nu_t} \frac{df_{\theta-}(x_t; t)}{dt}$. For $\lambda \in (0, 1)$, the objective $\|f_\theta(x_t; t) - f_{\theta-}(x_{\lambda t}; \lambda t)\|_2^2$ yields consistency along the geometric sequence $\mathcal{T}_\lambda(t) = \{\lambda^k t\}_{k=0}^N$.

Define

$$g_t(x_t) = (x_t - \alpha_t f_t(x_t)) \sigma_t^{-1}.$$

Then, when $f_t(x_t) = x$, it follows that $g_t(x_t) = z$ for $x_t = \alpha_t x + \sigma_t z$. Using this, the flow map can be formulated in a DDIM-like manner as

$$f_{t,s}(x_t) = \alpha_s f_t(x_t) + \sigma_s g_t(x_t) = \frac{\sigma_s}{\sigma_t} x_t + (\alpha_s - \frac{\sigma_s}{\sigma_t} \alpha_t) f_t(x_t).$$

Assuming the composition chain

$$f_{s,r}(f_{t,s}(x_t)) = f_{s,r}(\tilde{x}_s) = \frac{\sigma_r}{\sigma_s} \tilde{x}_s + (\alpha_r - \frac{\sigma_r}{\sigma_s} \alpha_s) f_s(\tilde{x}_s),$$

for $\tilde{x}_s = f_{t,s}(x_t)$, we obtain

$$f_{t,r}(x_t) - f_{s,r}(f_{t,s}(x_t)) = (\alpha_r - \frac{\sigma_r}{\sigma_s} \alpha_s)(f_t(x_t) - f_s(\tilde{x}_s)).$$

For $s = \lambda^k t$ for some $k \in \mathbb{N}$, if it follows that $\tilde{x}_s = f_{t,s}(x_t) \approx x_s$, then $f_s(x_s) = f_t(x_t)$ and $f_{t,r} = f_{s,r} \circ f_{t,s}$. In this case, the flow map can be constructed along the geometric sequence $\mathcal{T}_\lambda(t)$.

In general, the velocity of the DDIM map is given by $\frac{d}{ds} f_{t,s} = \alpha'_s f_t + \sigma'_s g_t$. Since the unconditional velocity is

$$v_t^*(x_t) = \alpha'_t \mathbb{E}_{x|x_t}[x] + \sigma'_t \mathbb{E}_{x|x_t}[(x_t - \alpha_t x) \sigma_t^{-1}],$$

the DDIM map coincides with the flow map only when $v_s^*(f_{t,s}(x_t)) = \frac{d}{ds} f_{t,s}(x_t)$, which implies $\mathbb{E}_{x|\tilde{x}_s}[x] = f_t(x_t)$. Setting $s \rightarrow t$ reduces this condition to $\mathbb{E}_{x|x_t}[x] = f_t(x_t)$ by the identity assumption. However, this condition fails to preserve the injectivity of the flow map at $t = 1$ due to the mean collapse problem, thereby leading to a contradiction. Therefore, the DDIM-style map does not generally coincide with the flow map. \square

Reflow. Rectified flows introduce Reflow to straighten trajectories after training. In Reflow, sampling from the trained model is performed via

$$x_0 = x_1 + \int_1^0 v_\theta(x_t; t) dt \approx \text{ODESolver}(v_\theta, x_1, 1, 0),$$

followed by the finetune w.r.t. the coupling $\Pi_{Z,\theta} = p_Z(z)p_{v_\theta}(x|z)$. The velocity \hat{v}_t of the trajectory induced by the coupling $\Pi_{Z,\theta}$ is given by

$$\hat{v}_t = x_1 - \left(x_1 + \int_1^0 v_\theta(x_t; t) dt \right) = \int_0^1 v_\theta(x_t; t) dt,$$

which corresponds to the displacement of the flow map. Therefore, Reflow can be interpreted as direct supervision of the flow map under linear interpolation.

A.6. Suboptimality of direct training

Unlike Eulerian distillation, direct training does not guarantee convergence to the optimal flow map. Consider the direct training objective using the conditional velocity:

$$\mathcal{L}_{\text{DT}} = \mathbb{E}_{x,z,t,s} \left[\|\partial_t f_\theta(x_t; t, s) + v(x_t|x) \cdot \nabla_x f_\theta(x_t; t, s)\|_2^2 \right].$$

By defining the velocity error as $\Delta v = v_t(x_t|x) - v_t^*(x_t)$, we can rewrite the objective in the form of Eulerian Distillation:

$$\begin{aligned} \mathcal{L}_{\text{DT}} &= \mathbb{E}_{x,z,t,s} \left[\|\partial_t f_\theta(x_t; t, s) + (\Delta v + v_t^*(x_t)) \cdot \nabla_x f_\theta(x_t; t, s)\|_2^2 \right] \\ &= \mathbb{E}_{x,z,t,s} \left[\|\partial_t f_\theta(x_t; t, s) + \Delta v \cdot \nabla_x f_\theta(x_t; t, s) + v_t^*(x_t) \cdot \nabla_x f_\theta(x_t; t, s)\|_2^2 \right] \\ &= \mathbb{E}_{x,z,t,s} \left[\|\partial_t f_\theta(x_t; t, s) + v_t^*(x_t) \cdot \nabla_x f_\theta(x_t; t, s)\|_2^2 \right] + \mathbb{E}_{x,z,t,s} \left[\|\Delta v \cdot \nabla_x f_\theta(x_t; t, s)\|_2^2 \right], \end{aligned}$$

by the law of total variance since other terms are independent of x , and $\mathbb{E}_{x|x_t}[\Delta v] = 0$. In this case, the second term can be represented as

$$\mathbb{E}_{x,z,t,s} \left[\text{Var}_{x|x_t} [\Delta v \cdot \nabla_x f_\theta(x_t; t, s)] \right].$$

Under an independent coupling, the velocity error $\Delta v = v_t(x_t|x) - v_t^*(x_t)$ is typically nonzero. Consequently, unless $\|\nabla_x f_\theta(x_t; t, s)\|$ collapses to zero, the objective function inherently contains a larger variance term compared to that of Eulerian distillation. To minimize the overall loss, the optimizer faces a trade-off involving this variance. This introduces a bias that distorts the learned flow map towards becoming flatter by an external force $\Delta v_t = v_t - v_t^* \perp \nabla_x f_\theta(x_t; t, s)$.

Note that for flow matching, even when the loss term $\mathbb{E}_{x,z,t}[\|v(x_t|x) - F_\theta(x_t; t)\|_2^2]$ is decomposed as follows

$$\mathbb{E}[\|\Delta v + v^*(x_t) - F_\theta(x_t; t)\|_2^2] = \mathbb{E}[\|v^*(x_t) - F_\theta(x_t; t)\|_2^2] + \text{Var}[\Delta v].$$

The variance term, $\text{Var}[\Delta v]$, is independent of the network. Therefore, it does not affect convergence to the global optimum.

Euler-Lagrange Equation. Since the gradients of Eulerian distillation and direct training differ, the optima obtained by gradient-based optimization can also diverge. To find and compare the optima of the direct training objective, we apply the Euler-Lagrange equation. The objective can be represented in the vector form as

$$\mathcal{L}_{\text{DT}} = \mathbb{E}_{x,z,t,s} [\|\partial_t f_{t,s}(x_t) + v(x_t|x)^T \nabla_x f_{t,s}(x_t)\|_2^2] = \iint_{\Omega} \rho_t(x_t) \mathbb{E}_{x,z,s|x_t} [\|\cdot\|_2^2] dx_t dt.$$

We set the conditional expectation as the Lagrangian,

$$L(f, \partial_t f, \nabla_x f) = \mathbb{E}_{x,z,s|x_t} [\|\partial_t f_{t,s}(x_t) + v(x_t|x)^T \nabla_x f_{t,s}(x_t)\|_2^2].$$

The corresponding Euler-Lagrange equation is

$$\frac{\partial L}{\partial f} - \partial_t \left(\frac{\partial L}{\partial (\partial_t f)} \right) - \nabla_x \left(\frac{\partial L}{\partial (\nabla_x f)} \right) = 0 \iff \mathbb{E}_{x,z,s|x_t} [\partial_t R + \nabla \cdot (vR)] = 0,$$

where the residue is defined as

$$R = \partial_t f_{t,s}(x_t) + v(x_t|x)^T \nabla_x f_{t,s}(x_t).$$

Letting $\Delta v = v(x_t|x) - v^*(x_t)$ and introducing the operator $L_* f = \partial_t f + (v_t^*)^T \nabla_x f$, the residue can be rewritten as $R = L_* f_{t,s} + \Delta v^T \nabla_x f_{t,s}$, so that

$$\begin{aligned} \mathbb{E}_{x|x_t} [\partial_t R] &= \partial_t \mathbb{E}_{x|x_t} [R] = \partial_t (L_* f_{t,s}), \\ \mathbb{E}_{x|x_t} [\nabla \cdot (vR)] &= \nabla \cdot \mathbb{E}_{x|x_t} [(v^* + \Delta v)(L_* f_{t,s} + \Delta v^T \nabla_x f_{t,s})] \\ &= \nabla \cdot (v^* L_* f_{t,s} + \mathbb{E}_{x|x_t} [\Delta v (\Delta v^T \nabla_x f_{t,s})]) \\ &= \nabla \cdot (v^* L_* f_{t,s} + \Sigma_{\Delta v|x_t} \nabla_x f_{t,s}). \end{aligned}$$

Therefore, the optimality condition becomes

$$\begin{aligned} \mathcal{E}\mathcal{L} &= \mathbb{E}_{x,z,s|x_t} [\partial_t R + \nabla \cdot (vR)] \\ &= \partial_t (L_* f_{t,s}) + \nabla \cdot (v_t^* L_* f_{t,s}) + \nabla \cdot (\Sigma_{\Delta v|x_t} \nabla_x f_{t,s}) = 0. \end{aligned}$$

If we assume the L^2 -adjoint of L_* to be $L^* f = -\partial_t f - \nabla \cdot ((v_t^*)^T f)$, the condition simplifies to

$$L^* L_* f_{t,s} - \nabla \cdot (\Sigma_{\Delta v|x_t} \nabla_x f_{t,s}) = 0 \iff \|L_* f\|_2^2 + \nabla \cdot (\Sigma_{\Delta v|x_t} \nabla_x f_{t,s}) = 0.$$

Thus, the optimum of the direct training arises precisely when the above condition is satisfied. When $\Sigma_{\Delta v|x_t} = \text{Cov}_{x|x_t}[v(x_t|x)] \rightarrow 0$, the condition reduces to $L_* f_{t,s} = 0$, which is equivalent to Eulerian distillation. In this case, the quadratic structure ensures convergence via PSD curvature at the global optimum. Otherwise, we consider two cases separately: (i) $L_* f_{t,s} \neq 0$ and $\nabla \cdot (\Sigma_{\Delta v|x_t} \nabla_x f_{t,s}) < 0$, (ii) $L_* f_{t,s} = 0$ and $\nabla \cdot (\Sigma_{\Delta v|x_t} \nabla_x f_{t,s}) = 0$.

In the first case, since the flow map is the unique solution to the Eulerian equation, $f_{t,s}$ is no longer a valid flow map as it does not satisfy the equation. If this scenario is admitted, in other words, if we assume the network can be optimized to satisfy $\nabla \cdot (\Sigma_{\Delta v|x_t} \nabla_x f_{t,s}) < 0$ by gradient-based methods, it corresponds to a suboptimal solution. Otherwise, if this scenario is rejected, indicating that the network cannot be optimized to satisfy $\nabla \cdot (\Sigma_{\Delta v|x_t} \nabla_x f_{t,s}) = 0$, likely due to excessive optimization complexity, the second case can hardly be regarded as a tractable or accessible solution. Therefore, the stable point of direct training either contains suboptimal solutions or remains practically inaccessible. \square

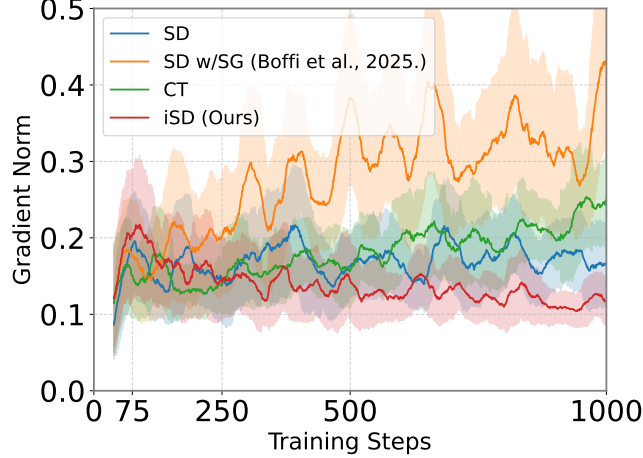


Figure 9. Gradient norms of each method. We estimate gradient norms under the same setting as Figure 2. *SD* denotes Eulerian self-distillation, *SD w/SG* denotes the stop-gradient version of ESD introduced by Boffi et al. (2025a), *CT* denotes the continuous-time consistency training objective, and *iSD* (Ours) denotes our improved Self-Distillation objective.

A.7. Instability of Consistency Training

The continuous-time consistency training objective employs a stop-gradient operation, ensuring that the main objective remains unchanged while improving computational efficiency. In this case, the objective is defined as

$$\mathcal{L}_{CT} = \mathbb{E}_{x,z,t,s} \left[f_{t,s}(x_t)^T \frac{df_{t,s}^-(x_t)}{dt} \right],$$

where $f_{t,s}(x_t) = f_\theta(x_t; t, s)$ and detaching gradient is denoted by $f_{t,s}^-(x_t) = f_{\theta^-}(x_t; t, s)$.

\mathcal{L}_{CT} reduces in value to Eulerian distillation even along the conditional trajectory, as demonstrated in Section A.5, paragraph on **sCT**. However, since the objective is expressed as a linear term, the Euler-Lagrange equation cannot determine a stationary point, as it contains no explicit terms of $f_{t,s}$ unless the gradient is detached:

$$\mathcal{E}\mathcal{L} = \mathbb{E}_{x,z,s|x_t} [L f_{t,s}^- + v_t^T \nabla_x f_{t,s}^-] = 0.$$

Moreover, while the quadratic term in Eulerian distillation ensures PSD curvature and provides stable convergence at the optimum, the consistency training objective does not enforce convergence, as the Hessian vanishes and the curvature required to stabilize the optimum is absent. It only specifies the fixed point on $L f_{t,s} = 0$, and the gradient dynamics alone may fail to converge.

Boffi et al. (2025b) also shows that fixed-point behavior can arise from stop-gradient operations by analyzing the formulation

$$\mathbb{E} [\|\partial_t f_{t,s} - v_t^T \nabla_x f_{t,s}^-\|_2^2].$$

This formulation differs in structure from the consistency-style objectives discussed above.

While they show that the functional gradient of this formulation can align with that of Eulerian distillation and admits fixed-point solutions, this analysis does not directly extend to prior consistency models, whose numerical realizations and optimization dynamics differ.

Motivated by this distinction, we formally analyze consistency-style objectives and show that they also admit fixed-point solutions satisfying the Eulerian equation, without guaranteeing global convergence under the PSD structure.

To highlight differences in numerical realization, we compare the gradient norms of each method on toy data, as shown in Figure 9. We observe that self-distillation with a stop-gradient applied to the spatial derivative can yield larger gradient norms than the original formulation, whereas our improved Self-Distillation yields consistently smaller gradient norms, which can help stabilize optimization.

□

A.8. Suboptimality of Network-Induced Coupling

For an arbitrary coupling $(\hat{x}, \hat{z}) \sim \Pi_{X,Z}$ with $\hat{x}_t = \alpha_t \hat{x} + \sigma_t \hat{z}$, the gap between the conditional and marginal velocities is given by

$$\Delta v = \hat{x}'_t - v_t^*(\hat{x}_t) = \alpha'_t(\hat{x} - \mu_{x|\hat{x}_t}) + \sigma'_t(\hat{z} - \mu_{z|\hat{x}_t}),$$

where $\mu_{x|x_t} = \mathbb{E}_{x|x_t}[x]$ and $\mu_{z|x_t} = \mathbb{E}_{z|x_t}[z]$ are conditional means. This follows since $v_t^*(x_t) = \mathbb{E}_{x|x_t}[v(x_t|x)]$ can be expressed as $\mathbb{E}_{x,z|x_t}[\alpha'_t x + \sigma'_t z]$. The general form of the loss can be expressed by

$$\mathbb{E}[\|A + g^T \Delta v\|_2^2] = \mathbb{E}[\|A\|_2^2] + 2\mathbb{E}[A^T g^T \Delta v] + \mathbb{E}[\|g^T \Delta v\|_2^2],$$

where $A = \partial_t f_{t,s}^\theta + g^T v_t^*(x_t)$ and $g = \nabla_x f_{t,s}^\theta$.

Case 1: Independent Coupling. In this setup, we use an independent coupling $(x, z) \sim p_{\text{data}} \times p_Z$ and the conditional velocity $v_t(x_t|x)$, which corresponds to setting $\hat{x} = x$ and $\hat{z} = z$. The velocity gap is $\Delta v = v_t(x_t|x) - v_t^*(x_t)$. The cross-term vanishes because the expectation of the gap is zero conditioned on x_t :

$$\mathbb{E}_{x,z|x_t}[\Delta v] = \mathbb{E}_{x,z|x_t}[v_t(x_t|x) - v_t^*(x_t)] = v_t^*(x_t) - v_t^*(x_t) = 0.$$

Thus, $2\mathbb{E}[A \Delta v \cdot g] = 0$ and the loss simplifies to

$$\mathcal{L}_{\text{IC}} = \mathcal{L}_{\text{ED}} + \mathbb{E}[\|g^T \Delta v\|_2^2] = \mathcal{L}_{\text{ED}} + \mathbb{E}[\text{Var}_{x|x_t}[g^T \Delta v]].$$

The variance term, which represents the error from Eulerian distillation, can be expanded as:

$$\begin{aligned} \mathcal{E}_{\text{IC}} &= \text{Var}_{x,z|x_t}[g^T(\alpha'_t(x - \mu_{x|x_t}) + \sigma'_t(z - \mu_{z|x_t}))] \\ &= (\alpha'_t)^2 g^T \Sigma_{x|x_t} g + (\sigma'_t)^2 g^T \Sigma_{z|x_t} g + 2\alpha'_t \sigma'_t g^T \Sigma_{xz|x_t} g, \end{aligned}$$

where $\Sigma_{x|x_t} = \text{Cov}_{x|x_t}(x, x)$, $\Sigma_{z|x_t} = \text{Cov}_{z|x_t}(z, z)$, and $\Sigma_{xz|x_t} = \text{Cov}_{x,z|x_t}(x, z)$.

Case 2: Generator-Induced Coupling. Generator-induced coupling methods replace one of the variables with a network prediction, $\hat{x} = f_{t,0}^\theta(x_t)$ with stop-gradient: $\hat{x}_t = \alpha_t f_{t,0}(x_t) + \sigma_t z$. For the first case, the velocity gap is:

$$\Delta v = \alpha'_t(f_{t,0}(x_t) - \mu_{x|\hat{x}_t}) + \sigma'_t(z - \mu_{z|\hat{x}_t}).$$

The conditional expectation of the gap is no longer zero in general:

$$\mathbb{E}_{z|x_t}[\Delta v] = \alpha'_t(f_{t,0}(x_t) - \mu_{x|\hat{x}_t}).$$

This introduces a non-zero cross-term in the loss, then the total error term for GC is:

$$\mathcal{E}_{\text{GC}} = 2\alpha'_t A^T g^T (f_{t,0}(x_t) - \mu_{x|\hat{x}_t}) + (\alpha'_t)^2 [g^T(f_{t,0}(x_t) - \mu_{x|\hat{x}_t})]^2 + (\sigma'_t)^2 g^T \Sigma_{z|x_t} g.$$

Comparing the error terms, we find that $\mathcal{E}_{\text{IC}} > \mathcal{E}_{\text{GC}}$ if:

$$(\alpha'_t)^2 g^T \Sigma_{x|x_t} g + 2\alpha'_t \sigma'_t g^T \Sigma_{xz|x_t} g > 2\alpha'_t A^T g^T (f_{t,0}(x_t) - \mu_{x|\hat{x}_t}) + (\alpha'_t)^2 [g^T(f_{t,0}(x_t) - \mu_{x|\hat{x}_t})]^2.$$

When the generator is a good estimator of the posterior mean, i.e., $f_{t,0}^\theta(x_t) \approx \mu_{x|\hat{x}_t}$, the right side becomes small. However, at $t = 1$, this condition reduced to $f_{1,0}^\theta(z) = \mu_{z|x} = \mu_Z$, as shown in Section A.1, which results in posterior mean collapse. In this case, $f_{1,0}^\theta$ becomes constant as \mathcal{E}_{GC} approaches zero, violating the injectivity required for a well-defined flow map, leading to a contradiction. Thus, while generator-induced coupling can reduce the error, it does not eliminate it entirely, and therefore does not guarantee convergence in continuous-time consistency training.

VCT (Silvestri et al., 2025) introduces an additional network $g : x \mapsto z$ for $\hat{x} = x$ and $\hat{z} = g(x)$. In this case, enforcing $g(x) \approx \mu_{z|x}$ can reduce the gap, but does not eliminate the whole, since the term $(\alpha'_t)^2 g^T \Sigma_{x|x_t} g$ remains. From a consistency training perspective, since the independent coupling already exhibits a marginal velocity field, this choice does not provide additional guarantees toward marginal velocity, although it can reduce the variance of the loss when g is a good posterior approximator. \square

A.9. Linearization Cost Hypothesis

Recall that $f_{t,s}^\theta(x_t) = \nu^{-1}(A'_{t,s}x_t - A_{t,s}F_{t,s}^\theta(x_t))$ for $A_{t,s} = \alpha_s\sigma_t - \sigma_s\alpha_t$. Under the given formulation of flow maps, a pseudo velocity network F_θ learns the weighted displacement between x_t and x_s . From the perspective of F_θ , this process can be seen as shifting the training target from a classical instantaneous velocity field to an average velocity field (a weighted displacement field), which transforms the path between x_t and x_s into the linear form of x_t and F_θ . We refer to it as *linearization*.

Differentiating with respect to the starting point t gives

$$\frac{df_\theta(x_t; t, s)}{dt} = \nu^{-1} \left(A''_{t,s}x_t + A'_{t,s}(v_t^*(x_t) - F_\theta(x_t; t, s)) - A_{t,s} \frac{dF_\theta(x_t; t, s)}{dt} \right).$$

Following AYF-EMD (Sabour et al., 2025), the gradient of the consistency training can be written as

$$\begin{aligned} & \nabla_\theta \mathbb{E} \left[2f_\theta^T(x_t; t, s) \frac{df_{\theta-}(x_t; t, s)}{dt} \right] \\ & \propto \nabla_\theta \mathbb{E} \left[-A_{t,s} \nu^{-2} F_\theta(x_t; t, s) \cdot \left(A''_{t,s}x_t + A'_{t,s}(v_t^*(x_t) - F_{\theta-}(x_t; t, s)) - A_{t,s} \frac{dF_{\theta-}(x_t; t, s)}{dt} \right) \right]. \end{aligned}$$

In this case, $v_t^* - F_\theta$ can be interpreted as the flow matching term weighted by $A'_{t,s}$, and $A''_{t,s}x_t - A_{t,s}dF_\theta/dt$ as a linearization term involving the JVP, which penalizes the t -dependent outputs of f_θ . For a linear interpolation, $A_{t,s}$ takes the form $A_{t,s} = t - s$, while for a trigonometric interpolation $A_{t,s} = \sin(t - s)$, both are proportional to $t - s$. As $s \rightarrow t$ and $(t - s) \rightarrow 0$, the contribution of the linearization term vanishes, while the flow matching term is amplified. Conversely, as $s \rightarrow 0$, the linearization term is amplified and the flow matching term diminishes.

We note that the linearization cost increases with step size, making optimization more challenging. This is because the linearization term involves a complex structure induced by the JVP, whereas the flow matching term requires only a simple forward pass. Such a complex structure may introduce additional fixed points or spikes, hindering convergence to the desired optimum. To demonstrate this hypothesis, we construct loss landscapes before and after time-condition relaxation in Section C.6, and observe that the relaxation reduces loss spikes and variances empirically.

A.10. Training-time Classifier-free Guidance

MeanFlow suggests Classifier-free Guidance (Ho & Salimans, 2021) (CFG) for flow maps:

$$\begin{aligned} & \nabla_\theta \mathbb{E} [\|F_\theta(x_t; t, s, c) - \text{sg}[\tilde{v}_t(x_t|x) - (t - s)(\tilde{v}_t(x_t|x) \cdot \nabla_x F_\theta + \partial_t F_\theta)]\|] \\ & \text{where } \tilde{v}_t(x_t|x) = F_{\theta-}(x_t; t, t, \emptyset) + \omega(v_t(x_t|x) - F_{\theta-}(x_t; t, t, \emptyset)), \end{aligned}$$

for a conditional class label c , the null class label \emptyset of unconditional generation, and a guidance scale ω . We find that this formulation encourages the flow map to follow the ground-truth CFG trajectory. The ground-truth CFG trajectory is given by $\tilde{v}_t^*(x_t; c) = v_t^*(x_t) + \omega(v_t^*(x_t; c) - v_t^*(x_t))$ where $v_t^*(x_t; c)$ is the class-conditional marginal velocity $v_t^*(x_t; c) = \mathbb{E}_{x|x_t, c}[v_t(x_t|x)]$ and $v_t^*(x_t)$ is the marginal velocity $v_t^*(x_t) = \mathbb{E}_{x|x_t}[v_t(x_t|x)] = \mathbb{E}_c[v_t^*(x_t; c)]$.

To prove this, we first consider only the flow matching setting:

$$\begin{aligned} & \nabla_\theta \mathbb{E} \left[\|F_\theta(x_t; t, c) - \tilde{v}_t(x_t|x)\|_2^2 \right] \\ & = \nabla_\theta \mathbb{E} \left[\|F_\theta(x_t; t, c) - (F_{\theta-}(x_t; t, \emptyset) + \omega(v_t(x_t|x) - F_{\theta-}(x_t; t, \emptyset)))\|_2^2 \right]. \end{aligned}$$

With label dropout $c = \emptyset$, the objective reduces to weighted unconditional flow matching that converges to the unconditional marginal velocity:

$$\begin{aligned} & \nabla_\theta \mathbb{E} \left[\|F_\theta(x_t; t, \emptyset) - (F_{\theta-}(x_t; t, \emptyset) + \omega(v_t(x_t|x) - F_{\theta-}(x_t; t, \emptyset)))\|_2^2 \right] \\ & = \mathbb{E} [2\omega \cdot \nabla_\theta F_\theta(x_t; t, \emptyset) \cdot (F_{\theta-}(x_t; t, \emptyset) - v_t(x_t|x))] \\ & = \nabla_\theta \mathbb{E} \left[\omega \|F_\theta(x_t; t, \emptyset) - v_t(x_t|x)\|_2^2 \right]. \end{aligned}$$

In this case, we can set $F_\theta(x_t; t, \emptyset) \approx v_t^*(x_t)$ if the network has sufficient capacity. For the conditional case $c \neq \emptyset$, applying the tower property yields:

$$\begin{aligned}
 & \nabla_\theta \mathbb{E} \left[\|F_\theta(x_t; t, c) - (F_\emptyset(x_t; t) + \omega(v_t(x_t|x) - F_\emptyset(x_t; t)))\|_2^2 \right] \\
 &= \nabla_\theta \mathbb{E} \left[\mathbb{E}_{x|x_t, c} \left[\|F_\theta(x_t; t, c) - (F_\emptyset(x_t; t) + \omega(v_t(x_t|x) - F_\emptyset(x_t; t)))\|_2^2 \right] \right] \\
 &= \nabla_\theta \mathbb{E} \left[\mathbb{E}_{x|x_t, c} \left[\|F_\theta(x_t; t, c) - (F_\emptyset(x_t; t) + \omega(v_t^*(x_t; c) - v_t^*(x_t; c) + v_t(x_t|x) - F_\emptyset(x_t; t)))\|_2^2 \right] \right] \\
 &= \nabla_\theta \mathbb{E} \left[\mathbb{E}_{x|x_t, c} \left[\|F_\theta(x_t; t, c) - (F_\emptyset(x_t; t) + \omega(v_t^*(x_t; c) - F_\emptyset(x_t; t))) + \omega(v_t^*(x_t; c) - v_t(x_t|x))\|_2^2 \right] \right] \\
 &\approx \nabla_\theta \mathbb{E} \left[\|F_\theta(x_t; t, c) - (v_t^*(x_t) + \omega(v_t^*(x_t; c) - v_t^*(x_t)))\|_2^2 \right] + \omega^2 \cdot \nabla_\theta \mathbb{E} [\text{Var}_{x|x_t, c} [v_t(x_t|x)]] \\
 &= \nabla_\theta \mathbb{E} \left[\|F_\theta(x_t; t, c) - \tilde{v}_t^*(x_t; c)\|_2^2 \right],
 \end{aligned}$$

where $F_\emptyset(x_t; t) = F_{\theta-}(x_t; t, \emptyset)$ for brevity. Thus, the self-referential target $\tilde{v}_t(x_t|x)$ with label dropout ensures convergence to the ground-truth CFG velocity.

Consider the convergence of the flow map to the CFG velocity field. Following Section A.5, let $L_* f_{t,s} = \partial_t f_{t,s} + \tilde{v}_t^* \cdot \nabla_x f_{t,s}$ and $\Delta v = \tilde{v}_t(x_t|x) - \tilde{v}_t^*(x_t; c)$. It is sufficient to show that $\mathbb{E}_{x|x_t, c} [\Delta v] = 0$, and it is guaranteed when label dropout is applied, and the flow matching objective is jointly optimized. Thus, the objective encourages convergence to the flow map induced by the CFG velocity. \square

B. Improving Self-Distillation

B.1. Guarantee the Convergence

Revisit our objective

$$\mathcal{L} = \mathbb{E}_{x,z,t,s} \left[\|F_{t,t}^\theta(x_t; t, t) - v_t(x_t|x)\|_2^2 + \left\| \partial_t f_{t,s}^\theta(x_t) + F_{t,t}^{\theta-}(x_t) \cdot \nabla_x f_{t,s}^\theta(x_t) \right\|_2^2 \right].$$

The first term of the right side trains $F_{t,t}^\theta(x_t)$ to approximate the marginal velocity via the flow matching objective, while the second term learns the flow map $f_{t,s}$ along the trajectory of $F_{t,t}^{\theta-}$ in a self-distillation manner.

Individually, each term is guaranteed to converge to its desired optimum, the marginal velocity and the flow map of the velocity $F_{t,t}^{\theta-}$ by the Eulerian equation (Section A.3). From a joint perspective, we need to consider $t = s$, since the network is forced to optimize both terms simultaneously at this point. As Eulerian distillation collapses to the flow matching objective when $t \rightarrow s$, the second term trains the model to learn the instantaneous velocity of the trajectory (Section A.9). In this case, $F_{t,t}^\theta$ learns from $F_{t,t}^{\theta-}$, and inductively approximates $v_t^*(x_t)$ through the first term. This naturally reduces to a non-conflict joint training. For $t \neq s$, the network is conditioned differently in the two terms, and it can learn the proper mapping provided that the network capacity is sufficient. Consequently, the overall objective trains the network to follow the marginal velocity as the trajectory of the flow map naturally. \square

B.2. Deriving Final Objective

Recall the consistency training objective under the flow map representation (Section A.9):

$$\begin{aligned}
 & \nabla_\theta \mathbb{E} \left[2f_\theta^T(x_t; t, s) \frac{df_{\theta-}(x_t; t, s)}{dt} \right] \\
 & \propto \nabla_\theta \mathbb{E} \left[-A_{t,s} \nu^{-2} F_\theta(x_t; t, s) \cdot \left(A_{t,s}'' x_t + A_{t,s}' (v_t^*(x_t) - F_{\theta-}(x_t; t, s)) - A_{t,s} \frac{dF_{\theta-}(x_t; t, s)}{dt} \right) \right] \\
 &= A_{t,s} \nu^{-2} \cdot \nabla_\theta \mathbb{E} [\|F_\theta(x_t; t, s) - \text{sg}[F_{\text{tgt}}(x_t; t, s)]\|_2^2],
 \end{aligned}$$

where $F_{\text{tgt}}(x_t; t, s) = F_\theta(x_t; t, s) + \left(A_{t,s}'' x_t + A_{t,s}' (v_t^*(x_t) - F_\theta(x_t; t, s)) - A_{t,s} \frac{dF_\theta(x_t; t, s)}{dt} \right)$.

To follow the marginal velocity, we replace $v_t^*(x_t)$ with instantaneous velocity $F_{t,t}^\theta(x_t)$ while jointly training with \mathcal{L}_{CFM} . Particularly, for linear interpolation, we have $A_{t,s} = t - s$, $A_{t,s}' = 1$ and $A_{t,s}'' = 0$. This simplifies the target to

$F_{\text{tgt}}^{\text{lin}}(x_t; t, s) = v_t^*(x_t) - (t - s)F'_\theta(x_t; t, s)$ which coincides with the regression target of MeanFlow. For trigonometric interpolation, we have $A_{t,s} = \sin(t - s)$, $A'_{t,s} = \cos(t - s)$ and $A''_{t,s} = -\sin(t - s)$. Thus, the target becomes $F_{\text{tgt}}^{\text{tri}} = F_\theta(x_t; t, s) + \cos(t - s) \cdot (v_t^*(x_t) - F_\theta(x_t; t, s)) - \sin(t - s) \cdot (x_t + F'_\theta(x_t; t, s))$.

Although consistency training already guarantees the marginal flow map at its fixed point, the gradient in practice can exhibit a gap expressed as:

$$\mathbb{E}_{x,z,t,s}[f_{t,s}^\theta(\Delta v \cdot \nabla_x f_{t,s}^{\theta^-})].$$

When self-distillation is combined with flow matching, $\mathbb{E}[\|F_\theta(x_t; t, t) - v_t(x_t | x)\|_2^2]$, the velocity error $\Delta v = F_\theta(x_t; t, t) - v_t^*(x_t)$ can be further reduced compared to $\Delta v = v_t(x_t | x) - v_t^*(x_t)$, thereby stabilizing the training. In Section C.6, we demonstrate that self-distillation empirically reduces loss variance through loss landscape analysis.

For JVP approximation, to ensure that dx_t/dt follows the velocity $v_\theta(x_t; t) = F_{t,t}^\theta(x_t)$, we approximate

$$\frac{dx_t}{dt} \approx \frac{[x_t + \epsilon \cdot v_\theta(x_t; t)] - [x_t - \epsilon \cdot v_\theta(x_t; t)]}{2\epsilon} = v_\theta(x_t; t).$$

Thus, the full JVP approximation becomes

$$\frac{dF_\theta(x_t; t, s)}{dt} = \frac{F_\theta(x_t + \epsilon \cdot v_\theta(x_t; t), t + \epsilon, s) - F_\theta(x_t - \epsilon \cdot v_\theta(x_t; t), t - \epsilon, s)}{2\epsilon} + O(\epsilon^2).$$

Our final objective is

$$\begin{aligned} \mathcal{L}_{\text{iSD}} &= \lambda_1 \mathcal{L}_{\text{CFM}} + \lambda_2 \mathcal{L}_{\text{SD-R}}, \\ \mathcal{L}_{\text{CFM}} &= \mathbb{E}[\|F_\theta(x_t; t, t) - v_t(x_t | x)\|_2^2], \quad \mathcal{L}_{\text{SD-R}} = \mathbb{E}[\|F_\theta(x_t; t, s) - \text{sg}[F_{\text{tgt}}(x_t; t, s)]\|_2^2]. \end{aligned}$$

We consider two weighting methods: (i) cosine weighting $\lambda_1 = \lambda_2 = \cos(\pi t/2)$ from Sun et al. (2025), and (ii) adaptive weighting $\lambda_1 = \lambda_2 = (\text{sg}[\tilde{\mathcal{L}}_{t,s}(x_t, x)] + \eta)^{-p}$ where $\tilde{\mathcal{L}}_{t,s}(x_t, x) = \|F_\theta(x_t; t, t) - v_t(x_t | x)\|_2^2 + \|F_\theta(x_t; t, s) - \text{sg}[F_{\text{tgt}}(x_t, t, s)]\|_2^2$ from Geng et al. (2025a). While our method is sufficiently stable to train flow maps without additional weighting, we found that adaptive weighting can further improve performance in the SD-VAE setting, and cosine weighting in the VA-VAE setting. We use adaptive weighting by default, except when using VA-VAE.

When using JVP approximation, the resulting asymptotic error is bounded by $O(\epsilon^2)$. This error appears acceptable under BF16 precision, as the approximation shows better results than direct JVP computation. The complete training and sampling algorithms are provided in Algorithm 1 and Algorithm 2.

Algorithm 1 (iSD Training) Training algorithm of vanilla iSD

Input: Noise distribution p_Z , data distribution p_X , model F_θ , learning rate μ , time distribution τ , adaptive weighting (η, p) , JVP approximation step size ϵ , class labels c

repeat

$$\begin{aligned} z &\sim p_Z, \quad x \sim p_X, \quad t, s \leftarrow \tau \\ x_t &\leftarrow \alpha_t x + \sigma_t z, \quad v_t \leftarrow \alpha'_t x + \sigma'_t x \\ F_{t,s} &\leftarrow F_\theta(x_t; t, s, c), \quad F_{t,t} \leftarrow F_\theta(x_t; t, t, c) \\ F'_{t,s} &\leftarrow [F_\theta(x_t + \epsilon F_{t,t}; t + \epsilon, s, c) - F_\theta(x_t - \epsilon F_{t,t}; t - \epsilon, s, c)] / (2\epsilon) && \triangleright \text{JVP-Approx.} \\ F_{\text{tgt}} &\leftarrow F_{t,s} + (A''_{t,s} x_t + A'_{t,s} (F_{t,t} - F_{t,s}) - A_{t,s} F'_{t,s}) \\ \mathcal{L} &\leftarrow \lambda_1 \|F_{t,t} - v_t\|_2^2 + \lambda_2 \|F_{t,s} - \text{sg}[F_{\text{tgt}}]\|_2^2 && \triangleright \text{Optimization Target} \\ \theta &\leftarrow \theta - \mu \nabla_\theta \mathcal{L} && \triangleright \text{Model Update} \end{aligned}$$

until Convergence

B.3. Random initialization instead of Preconditioners

When constructing the iSD framework, we focus on random initializations rather than preconditioners. As shown in Table 2, pretrained networks with better FIDs do not necessarily yield better FIDs in the resulting consistency models. With random initialization, one can explore different random seeds and retrain the network to obtain improved results. There also

Algorithm 2 (iSD Sampling) Sampling algorithm of vanilla iSD

```

Input: Initial noise  $z \sim p_Z$ , trained model  $F_\theta$ , class labels  $c$ , sampling time steps  $\{t_i\}_{i=1}^N$ 
 $x \leftarrow z$ 
for  $i \leftarrow 1$  to  $N$  do
     $x \leftarrow \cos(t_{i+1} - t_i) \cdot x + \sin(t_{i+1} - t_i) \cdot F_\theta(x; t_i, t_{i+1}, c)$ 
end for

```

remains potential to improve performance using alternative initialization strategies, such as leveraging preconditioners. However, when adopting preconditioners as baselines, it becomes difficult to systematically design experiments to discover *better preconditioners*: which data, architectures, and hyperparameters should be used, how to quantify the quality of preconditioners, and whether perturbing pretrained weights is necessary. Therefore, we conclude that random initialization makes the reproducibility problem more tractable, and we construct the iSD as a reproducible, randomly initializable framework.

B.4. Classifier-free Guidance of Flow Map Models

Pre-CFG. By abstracting the guiding trajectory to v_θ , the flow map model can naturally be trained to follow the specific trajectory as long as it is Lipschitz continuous. To achieve this, we replace the guiding trajectory and refer to this training scheme as *Pre-CFG*. We consider three variants of objectives: iSD-C, iSD-U, and iSD-T.

iSD-U (Guidance-Unconditional). Given a label c and a null class label \emptyset , let the corresponding velocity fields be $F_{t,t}(x_t; c)$ and $F_{t,t}(x_t; \emptyset)$. If both are globally Lipschitz continuous, then the CFG trajectory $\tilde{v}_\theta(x_t; t, c) = \tilde{v}_t(x_t; c)$ is also globally Lipschitz continuous, since any linear combination of Lipschitz continuous functions remains Lipschitz continuous.

$$\tilde{v}_\theta(x_t; t, c) = F_\theta(x_t; t, t, \emptyset) + \omega(F_\theta(x_t; t, t, c) - F_\theta(x_t; t, t, \emptyset)).$$

Thus, the flow map can be trained to follow the CFG velocity field. As a naive approach, we first train the network $F_{t,s}^\theta(x_t; c)$ to align with \tilde{v}_θ , while leaving the remaining components unchanged. This shares a similar scheme with the Shortcut Model, which trains the marginal velocity and guides the shortcut mapping with a constructed CFG trajectory \tilde{v}_θ .

iSD-C (Guidance-Conditional). In this case, however, we need to address a conflict: \mathcal{L}_{CFM} enforces $F_{t,t} \approx v_t^*$ while $\mathcal{L}_{\text{SD-R}}$ enforces $F_{t,t} \approx \tilde{v}_\theta$. To resolve this, we append the guidance scale ω as an additional condition, $F_{t,t}^\theta(x_t; c, \omega)$. Then, the modified objectives are given by:

$$\begin{aligned} \mathcal{L}_{\text{CFM}} &= \mathbb{E} \left[\|F_\theta(x_t; t, t, c, 1.0) - v_t(x_t | x)\|_2^2 \right], \\ \mathcal{L}_{\text{iSD-C}} &= \mathbb{E} \left[\|F_\theta(x_t; t, s, c, \omega) - \text{sg}[F_{\text{tgt}}(x_t; t, s, c, \omega)]\|_2^2 \right], \end{aligned}$$

where

$$\begin{aligned} F_{\text{tgt}} &= F_{t,s}(x_t; c, \omega) + (A_{t,s}''x_t + A_{t,s}'(\tilde{v}_t(x_t; c) - F_{t,s}(x_t; c, \omega)) - A_{t,s}F_{t,s}'(x_t; c, \omega)), \\ \tilde{v}_t(x_t; c) &= F_{t,t}(x_t; \emptyset, 1.0) + \omega(F_{t,t}(x_t; c, 1.0) - F_{t,t}(x_t; \emptyset, 1.0)), \end{aligned}$$

with θ omitted for brevity. Hence, \mathcal{L}_{CFM} ensures $F_{t,t}(x_t; c, 1.0) \approx v_t^*(x_t; c)$, while $\mathcal{L}_{\text{iSD-C}}$ ensures $F_{t,t}(x_t; c, \omega) \approx \tilde{v}_t(x_t; c)$. This choice is natural, as $\tilde{v}_t = v_t^*$ when $\omega = 1$.

iSD-T (Training-time CFG). To resolve the conflict from another perspective, we adopt the training-time CFG described in Section A.10. As proven there, the training target $\tilde{v}_t(x_t | x) = (1 - \omega)F_{\theta-}(x_t; t, t, \emptyset) + \omega v_t(x_t | x)$ guarantees the convergence of flow matching networks to the CFG velocity field. Accordingly, we modify the flow matching objective to follow the CFG velocity, distilling the approximated velocity into flow mappings:

$$\begin{aligned} \mathcal{L}_{\text{CFM}} &= \mathbb{E} \left[\|F_\theta(x_t; t, t, c) - \tilde{v}_t(x_t | x)\|_2^2 \right], \\ \mathcal{L}_{\text{iSD-T}} &= \mathbb{E} \left[\|F_\theta(x_t; t, s, c) - \text{sg}[F_{\text{tgt}}(x_t; t, s, c)]\|_2^2 \right]. \end{aligned}$$

where $v_\theta(x_t; t) = F_\theta(x_t; t, t, c)$. In this case, the network approximates the CFG velocity, and the resulting flow mappings naturally follow the CFG trajectory. Unlike $\mathcal{L}_{\text{iSD-U}}$, the network does not compromise theoretical guarantees at $s = t$. We

finalize our method by adopting iSD-T as the default configuration. The ablation studies are provided in Section C.3, and the training algorithm is described in Algorithm 3.

Post-CFG. However, *Post-CFG* defined as

$$\tilde{F}_\theta(x_t; t, s, c) = F_\theta(x_t; t, s, \emptyset) + \omega(F_\theta(x_t; t, s, c) - F_\theta(x_t; t, s, \emptyset)),$$

following Algorithm 4, does not follow the CFG trajectory. This discrepancy arises from the definition of the flow map,

$$f_\theta(x_t; t, s) = x_t + \int_t^s v_\tau^*(x_\tau) d\tau,$$

which performs the path integral along a specific trajectory induced by v_τ^* . For a CFG trajectory, the path integral should be taken along \tilde{v}_τ . In contrast, Post-CFG computes two separate forward passes, integrating along $v_\tau^*(x_\tau; c)$ and $v_\tau^*(x_\tau; \emptyset)$, rather than along \tilde{v}_τ . As a result, the integration differs from the expected CFG trajectory.

Algorithm 3 (iSD-T Training) Training algorithm of iSD-T

Input: Noise distribution p_Z , data distribution p_X , model F_θ , learning rate μ , time distribution τ , adaptive weighting (η, p) , JVP approximation ϵ , Pre-CFG scale ω , class labels c .

repeat

$z \sim p_Z, \quad x \sim p_X, \quad t, s \leftarrow \tau$	
$x_t \leftarrow \alpha_t x + \sigma_t z, \quad v_t \leftarrow \alpha'_t x + \sigma'_t z$	
$\tilde{v}_t = \omega v_t + (1 - \omega) F_\theta(x_t; t, t, \emptyset)$	
$F_{t,s} \leftarrow F_\theta(x_t; t, s, c), \quad F_{t,t} \leftarrow F_\theta(x_t; t, t, c)$	
$F'_{t,s} \leftarrow [F_\theta(x_t + \epsilon F_{t,t}; t + \epsilon, s, c) - F_\theta(x_t - \epsilon F_{t,t}; t - \epsilon, s, c)] / (2\epsilon)$	▷ JVP-Approx.
$F_{tgt} \leftarrow F_{t,s} + (A''_{t,s} x_t + A'_{t,s} (F_{t,t} - F_{t,s}) - A_{t,s} F'_{t,s})$	
$\mathcal{L} \leftarrow \lambda_1 \ F_{t,t} - \tilde{v}_t\ _2^2 + \lambda_2 \ F_{t,s} - \text{sg}[F_{tgt}]\ _2^2$	▷ Optimization Target
$\theta \leftarrow \theta - \mu \nabla_\theta \mathcal{L}$	▷ Model Update

until Convergence

Algorithm 4 (Post-CFG Sampling) Sampling algorithm of iSD with Post-CFG

Input: Initial noise $z \sim p_Z$, model F_θ , Post-CFG scale ω , class labels c , sampling steps $\{t_i\}_{i=1}^N$.

$x \leftarrow z$

for $i \leftarrow 1$ to N **do**

$\tilde{F}_{t,s} \leftarrow (1 - \omega) F_\theta(x; t_i, t_{i+1}, \emptyset) + \omega F_\theta(x; t_i, t_{i+1}, c)$	▷ Post-CFG
$x \leftarrow \nu^{-1} (A'_{t_i, t_{i+1}} x - A_{t_i, t_{i+1}} \tilde{F}_{t,s})$	

end for

C. Experimental Details

C.1. Reproducibility of Consistency Training

To evaluate the reproducibility of consistency training, we conducted experiments within the UCGM (Sun et al., 2025) framework. We compared the FID scores of several models trained under different initialization conditions. Following UCGM, we first extract latent representations of ImageNet-1K 256×256 using VA-VAE (Yao et al., 2025). All few-step models were trained with the same hyperparameters and settings: RAdam optimizer with a learning rate of 1e-4, weight decay of 0.0, $\beta_1 = 0.9$, $\beta_2 = 0.999$, batch size of 1024, gradient clipping at 0.1, and timestep t sampled from Beta(0.8, 1.0). For enhancement, we applied a label drop ratio of 0.1, an enhancement range of (0, 0.75), and a ratio of 2.0. We also used the cosine function as the loss weighting function and trained all models with linear interpolation for 40K iterations.

Multistep Baseline. We trained the DiT-XL/1 architecture initialized from the publicly released multistep checkpoint of UCGM. This configuration achieved a 2-step FID of 2.52, which is reasonable but still falls short of the reported FID 1.42.

LightningDiT. We trained the LightningDiT-XL/1 architecture from its released pretrained model. In this setting, the model achieved a 2-step FID of 9.59, which is worse than the reported FID.

In-house Multistep Model. We trained the DiT-XL/2 architecture from scratch. For training, we used AdamW (Loshchilov & Hutter, 2019) with a learning rate of 0.0002, $\beta_1 = 0.9$, $\beta_2 = 0.95$, EMA decay weight of 0.999, and timestep t sampled from Beta(1, 1). We used an enhancement ratio of 0.47 and a cosine weighting function. After training the multistep model for 800k iterations, we conducted consistency training under the same few-step settings. This resulted in a 2-step FID 5.78.

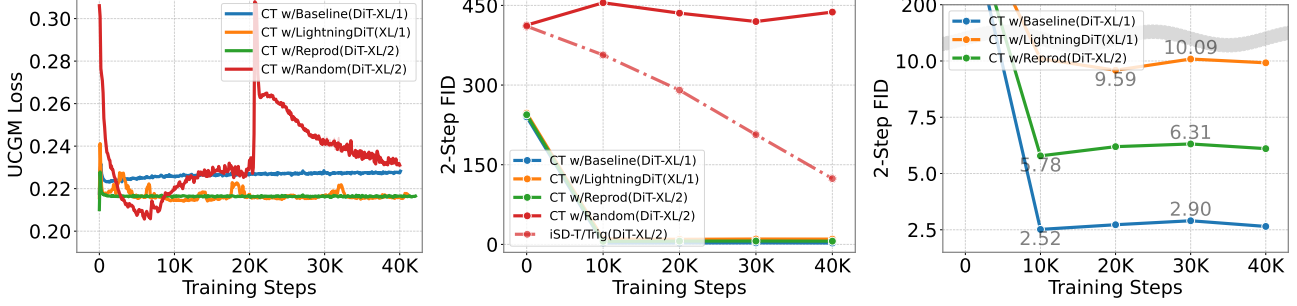


Figure 10. Training curves of consistency training. (a) Training loss over training steps. (b) Two-step FIDs over training steps. (c) Rescaled Y-axis for the consistency model with a preconditioner.

Without Preconditioner. We train a DiT-XL/2 architecture from randomly initialized weights without any preconditioner. In this case, training consistently failed, with the loss diverging and no meaningful samples being generated. While 40K steps may appear insufficient for scratch training, other scratch training methods already show a rapid decrease by 40K steps (Figure 10). We consider that this is enough to check the unstable dynamics compared to other models.

These suggest that consistency training is highly sensitive to initialization and the choice of preconditioner. It becomes unstable under random initialization and requires a well-trained multistep model. Even when initialized with preconditioners, consistency training demonstrates limited robustness and reproducibility across different architectures and setups.

C.2. Implementation

Table 9. Experimental Settings

DATASET		IMAGENET-1K 256×256					CELEBA-HQ 256×256	
PREPROCESSOR	SD-VAE (ROMBACH ET AL., 2022)			SD-VAE	VA-VAE (YAO ET AL., 2025)		SD-VAE	
INPUT SIZE	32 × 32 × 4			32 × 32 × 4	16 × 16 × 32		32 × 32 × 4	
CONDITION	CLASS-CONDITIONAL			CONDITIONAL	CONDITIONAL		UNCONDITIONAL	
BACKBONE	DiT-B/4	DiT-B/2	DiT-L/2	DiT-XL/2	DiT-XL/2 [†]	DiT-XL/1 [†]	DiT-B/2	
PARAMS (M)	131	131	459	676	676	676	131	
DEPTH	12	12	24	28	28	28	12	
HIDDEN DIM	768	768	1024	1152	1152	1152	768	
HEADS	12	12	16	16	16	16	12	
PATCH SIZE	4×4	2×2	2×2	2×2	2×2	1×1	2×2	
INTERPOLATION	TRIGONOMETRIC			LINEAR	LINEAR	LINEAR	TRIGONOMETRIC	
SELF-DISTILLATION	$\mathcal{L}_{iSD\text{-}T}$			$\mathcal{L}_{iSD\text{-}T}$	$\mathcal{L}_{iSD\text{-}T}$	$\mathcal{L}_{iSD\text{-}T}$	\mathcal{L}_{iSD}	
JOINT TRAINING	ENABLED			ENABLED	ENABLED	ENABLED	ENABLED	
JVP	APPROXIMATION			APPROX.	APPROX.	APPROX.	APPROXIMATION	
WEIGHTING	ADAPTIVE			ADAPTIVE	ADAPTIVE	COSINE	ADAPTIVE	
ϵ	0.005			0.005	0.005	0.005	0.005	
p	1.0			1.0	1.0	-	1.0	
η	0.01			0.01	0.01	-	0.01	
PRE-CFG ω	3.0			4.5	4.5	5.0	-	
FP PRECISION	BF16			BF16	BF16	BF16	BF16	
BATCH SIZE	256			256	256	256	256	
LABEL DROPOUT	0.1			0.1	0.1	0.1	-	
OPTIMIZER	ADAMW (LOSHCHILOV & HUTTER, 2019)			NORMUON (LI ET AL., 2025)	NORMUON	NORMUON	ADAMW	
LR SCHEDULER	CONSTANT			CONSTANT	CONSTANT	CONSTANT	CONSTANT	
β_1	0.9			-	-	-	0.9	
β_2	0.999			0.95	0.95	0.95	0.999	
MOMENTUM	-			0.95	0.95	0.95	-	
LEARNING RATE	1E-4			5E-4	5E-4	5E-4	1E-4	
TRAINING STEPS	400K			800K	600K	600K	200K	
WEIGHT DECAY	0			0	0	0	0	
EMA DECAY	0.99995			0.99995	0.99995	0.99995	0.99995	

ImageNet 256×256. SD-VAE (Rombach et al., 2022) was used to encode images into a $32 \times 32 \times 4$ latent representation.

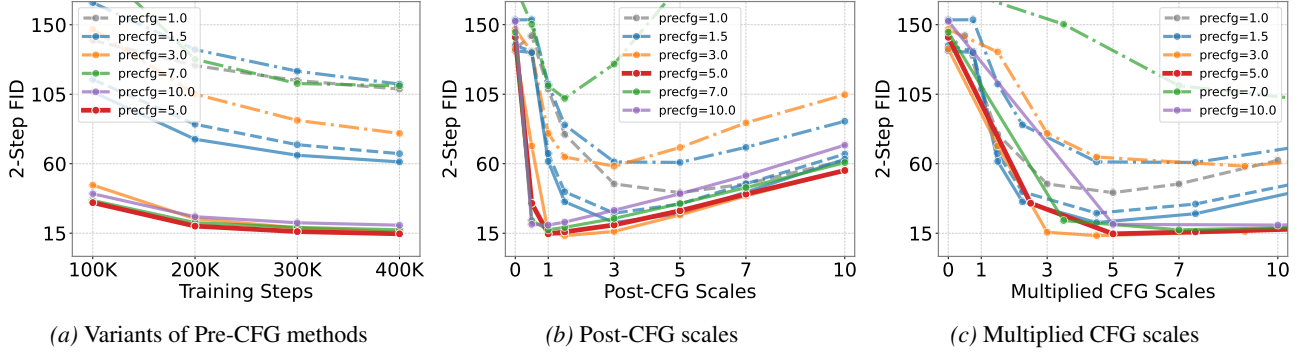


Figure 11. Variants of Pre-CFG. Dash, dash-dotted, and solid lines indicate iSD-U, iSD-C, and iSD-T, respectively. Each color represents a different Pre-CFG scale. Trigonometric interpolation and the JVP approximation are used by default on DiT-B/4. (on DiT-B/4a) FIDs of Pre-CFG variants over training steps. (b) FIDs of Post-CFG over guidance scales. (c) FIDs over multiplied guidance scales.

For DiT (Peebles & Xie, 2023) models, we employed RMSNorm (Zhang & Sennrich, 2019), QK normalization (Henry et al., 2020), and RoPE (Su et al., 2023) for minor improvements. Each model was scaled by depth and hidden dimension, while the patch size was kept fixed. We sampled t and s independently from Beta(0.8, 1.0), and set $t, s := \max(t, s), \min(t, s)$. For trigonometric interpolation, we additionally scale the timesteps as $t \leftarrow \frac{\pi}{2}t$ and $s \leftarrow \frac{\pi}{2}s$. For generations, we uniformly sampled the intermediate timesteps from the interval without additional engineering.

In ablation studies, DiT-B/4 was trained for 400K steps with a batch size of 256 and BF16 precision. For iSD-T with our final setting, the corresponding wall-clock time is 32 GPU hours on an A100. In scalability experiments, DiT-B/2 and DiT-XL/2 were trained for 400K steps, and DiT-XL/2 was further trained up to 800K steps for comparison with prior work, where the corresponding wall-clock time is 216 A100 GPU hours.

For completeness, we also report results obtained with additional performance-oriented architectural choices. Specifically, we augment the input space for the guidance scale and the CFG range by sampling them during training rather than using fixed values, following the design choices introduced in Geng et al. (2025b). The guidance scale is sampled from a truncated exponential distribution, and the CFG range is sampled from a uniform distribution. These modifications are orthogonal to our analysis and are used only to demonstrate that the proposed objective remains stable under commonly adopted performance-oriented settings. For conditioning, we concatenate conditions in the input token space. We denote this configuration with SD-VAE by DiT-XL/2 † and VA-VAE by DiT-XL/1 † . Detailed training parameters are provided in Table 9, and the corresponding results in Table 6 are reported under this setting.

CelebA-HQ. For CelebA-HQ, we use SD-VAE to encode images into $32 \times 32 \times 4$ latent representations. The model is based on DiT-L/2 in an unconditional setting, as in the Shortcut Model. It is trained on four RTX 3090 GPUs with a global batch size of 256. It takes 2 days for 200K steps (176 RTX 3090 GPU hours). Detailed settings are provided in Table 9.

C.3. Additional Ablation Study

JVP Approximation. To validate the effectiveness of JVP approximation, we not only apply the JVP approximation to iSD, but also to MeanFlow. With the direct JVP, the training requires approximately 25GB of VRAM and 58 A100 GPU hours under the ablation setting. After applying the approximation, the VRAM requirement reduces to 11GB and the wall-clock time to 21.5 GPU hours. The FID also decreases to 10.74, demonstrating a consistent decreasing trend.

Time-condition Annealing. Since our training dynamics can be divided into two stages: learning marginal velocity and flow mapping guided by itself, we also consider annealing of the time condition s , sampled near t for the initial stage and then warmed up to $0 \leq s < t$ as training continues. To linearly warm up the distribution of s , we first sample s and t following the baseline and reformulate s as:

$$s = t - (t - s) \times \min \left(1.0, \frac{\text{steps}}{\text{max_warmup}} \right).$$

We set max_warmup to 10K steps, corresponding to the first knee point of the flow matching term. However, time-condition annealing does not affect the training dynamics, and the resulting FID of 29.65 is even worse than the baseline.

To interpret this phenomenon, we consider two points: (i) we adopt adaptive weighting, which covers both flow matching and self-distillation objectives, and (ii) in the initial training stages, the loss of flow matching remains around 15, while that of self-distillation is near 0.5. This indicates that the flow matching objective already dominates the training signal, and thus the intended effect of annealing becomes diluted and negligible.

Variants of Pre-CFG. In the ablation setting, as shown in Figure 11a and Table 11, applying Pre-CFG \mathcal{L}_{iSD-U} with $\omega = 1.5$ improves FIDs compared to vanilla \mathcal{L}_{iSD} . However, training diverges when $\omega > 3.0$. This instability can be attributed to the conflict discussed in Section B.4, which disrupts optimal convergence as the guidance scale increases.

When the guidance scale is appended as a condition, \mathcal{L}_{iSD-C} enables training at higher guidance scales, outperforming \mathcal{L}_{iSD} . However, \mathcal{L}_{iSD-C} consistently underperforms \mathcal{L}_{iSD-U} . Intuitively, the additional condition forces the network to learn both CFG and non-CFG mappings, imposing an extra burden on the network. Even though \mathcal{L}_{iSD-U} compromises the theoretical guarantees at $s = t$, few-step generation commonly assumes $s \ll t$, resulting in comparable performance to iSD-T and making the issue negligible in practice. On the other hand, iSD-T neither introduces the conflict nor imposes additional burden on the network. It consistently outperforms both variants. Therefore, we adopt iSD-T as the default.

We also examined Post-CFG, as illustrated in Figure 11b. iSD-U shows improved results when Post-CFG is applied, particularly at $\omega = 3.0$. Applying Post-CFG on top of Pre-CFG can be viewed as applying CFG twice, resulting in a multiplied guidance scale. In this case, the total scale of iSD-U becomes $4.5 = 1.5 \times 3.0$. Similarly, iSD-T achieves its lowest FIDs around a Pre-CFG scale of $\omega = 5.0$, while Post-CFG on it underperforms even when the scale is close to one. When applying iSD-T with $\omega = 3.0$, Post-CFG outperforms at $\omega = 1.5$, corresponding to a total scale of 4.5. *These consistent observations suggest that the effective CFG scale lies near 5.0.* Based on these findings, we propose an ω -selection heuristic: measure FIDs using vanilla iSD with Post-CFG, and transfer the optimal Post-CFG scale to Pre-CFG.

iSD-C demonstrates effective CFG scales between 7.5-10.5, distinct from the ω -unconditional settings (iSD-U and iSD-T). However, even within its optimal range, iSD-C underperforms the unconditional variants. Since recent approaches adopt ω -conditioning in distillation, further investigation into scale selection remains a promising direction for future work.

Pre-CFG Scale for larger networks. For iSD-T, we investigate the effective guidance scale for the larger network, DiT-XL/2, as shown in Table 11. We train DiT-XL/2 with $\omega = 5.0$ and measure metrics across Post-CFG scales (Table 10).

Table 10. FIDs and ISs across Post-CFG scales for DiT-XL/2 with iSD-T ($\omega = 5.0$, 600K steps).

POST-CFG ω	0.0	0.5	1.0	1.5	3.0	5.0	7.0	10.0
FID	100.89	11.19	16.96	18.26	19.33	25.83	35.59	48.50
IS	13.53	164.48	234.85	229.35	181.94	116.25	85.75	65.36

DiT-XL/2 shows better results at the Post-CFG scale of $\omega = 0.5$, suggesting an effective Pre-CFG scale near 2.5. As reported in Table 11, the Pre-CFG scale of $\omega = 3.0$ outperforms $\omega = 5.0$, supporting the previously introduced heuristics. This indicates that *the effective Pre-CFG scale may not generalize to larger networks*. A similar trend has been observed in prior work, where different CFG scales were used across architectures.

Network-free Pre-CFG. Since iSD-T requires $F_{t,t}^\theta(x_t; \emptyset)$ for the modified flow matching target, it incurs additional network passes at every training step. To mitigate this, we explored replacing it with an analytic form of the marginal velocity:

$$v_t^*(x_t) = \sum_{x_i \in X} \left[\gamma_{t,i}(x_t) \cdot \frac{x_t - x_i}{t} \right], \quad \gamma_{t,i}(x_t) = \text{softmax}_i \left(\left\{ -\frac{x_t - (1-t)x_j}{2t} \right\}_{x_j \in X} \right),$$

where $\gamma_{t,i}$ denotes the posterior responsibility, and softmax_i represents the i -th output element of the softmax function over data points. However, this requires a full iteration over the dataset at every step, which becomes intractable for large datasets. To make training feasible, we approximate the marginal velocity by restricting the computation to a mini-batch $X_B \subset X$.

As a result, it plateaued at an FID of 343.7 and an IS of 1.0 even after 120K training steps under the consistency training setting, and at an FID of 261.1 and an IS of 1.927 under the iSD-T setting. We hypothesize that approximating the marginal velocity at the batch level introduces larger errors than the network approximation $F_{t,t}^\theta(x_t; \emptyset)$, thereby destabilizing the training process. Extending the training-time CFG to the 1-NFE setting remains future work.

C.4. Comparison with Other Work

CelebA-HQ. We conduct additional comparisons on CelebA-HQ to validate our method in an unconditional setting. For fair comparison, all methods in Figure 12 are trained with the DiT-B/2 architecture. As shown in Figure 12, iSD achieves competitive results on both few-step (4-step) and multi-step (128-step) generation. Since we train for 200K steps in this case, iSD provides an efficient training configuration, while the Shortcut Model uses 800K steps.

Shortcut Model. To compare the reproducibility with shortcut models, we train the network under the same ablation settings. We utilize an EMA network as a teacher with its CFG approach at $\omega = 1.5$. Note that its guidance method shares an idea with iSD-U (Section B.4). Under this setup, iSD-U attains stronger quantitative results, as shown in Table 11.

We hypothesize that the performance gap between the Shortcut Model and the iSD-U may arise from the step-size discretization in the Shortcut Model, which introduces an asymptotic gap relative to continuous-time formulations. Given the behaviors seen in iSD-U under different ω values, it is plausible that the Shortcut Model may experience increased training sensitivity as ω becomes larger. However, the training dynamics of shortcut models are stable enough that adaptive weighting is not necessary in this case. A Shortcut Model-like objective in a continuous-time setting may offer a more streamlined and stable alternative. Furthermore, as iSD-T shows the best results and provides solid theoretical grounding, applying the iSD-T Pre-CFG scheme to shortcut approaches provides a promising future direction.

FACM. As a concurrent work, FACM (Peng et al., 2025) suggests *flow-anchoring*, which jointly trains the network with the flow matching objective to provide an anchored training signal. This anchored signal is introduced to prevent degenerate model collapse and enable training from scratch. To compare with our method, we train FACM under our ablation settings. As shown in Table 11, FACM also reduces the variance of the resulting metrics compared to the baseline, and is on par with our methods in reproducibility. It can be viewed as a weak version of the time-condition relaxation, which relaxes the condition to $s \in \{0, t\}$ rather than $s = 0$. Not only does this align with our hypothesis, but Figure 14 also demonstrates that the joint training of flow matching reduces loss spikes and variance, making the training from scratch easier. This supports the effect of the flow-anchoring in the landspace perspective, and further supports our strong version of the relaxation.

improved MeanFlow. In line with recent work, improved MeanFlow (Geng et al., 2025b) reorganizes the MeanFlow identity into a v -loss formulation and highlights that conditional velocity leakage can arise when formalizing instantaneous velocities from average velocity (u -prediction). They note that this leakage contributes to training instability, and that replacing conditional velocity with the model’s own marginal velocity prediction can improve stability. Under linear interpolation, the resulting objective is structurally equivalent in form to a consistency-style self-distillation formulation. While the motivation and analytical perspective of Geng et al. (2025b) differ from ours, both approaches arrive at marginal velocity guidance through independent reasoning.

C.5. Policy Generation

To assess the applicability of iSD to diffusion-based policy learning, we train MeanFlow and iSD to imitate proficient human controls on two tasks, Push-T and Transport, using transformer- and state-based policies in simulation environments.

Unlike diffusion policy, iSD and MeanFlow require additional conditioning on s . Following prior work, which concatenates t to the observation context, we extend it by additionally appending s . Other settings follow prior work (Chi et al., 2023).

As shown in Table 8, iSD with linear interpolation achieves results comparable to those of other few-step methods, and particularly outperforms them on the Transport task. With 2-step sampling, iSD achieves performance comparable to that of the diffusion policy, which uses 100 sampling steps. Even with 2-step sampling, MeanFlow achieves an average success rate of 0.96, which is lower than iSD’s. This demonstrates that iSD can be a reasonable candidate for policy generation.

In Figure 13, we observe that iSD consistently exhibits higher action error than the other methods. However, it achieves success rates comparable to or better than those of other approaches. Even though the diffusion policy achieves a low action error of 0.004 on the Transport task, its peak success rate occurs earlier in training. In this case, the action error does not fully



Figure 12. 4-step samples from iSD on CelebA-HQ 256×256.

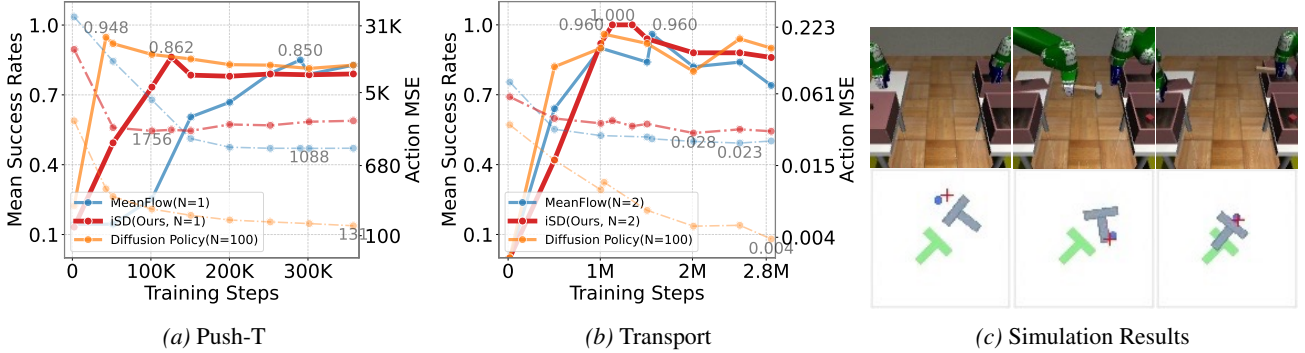


Figure 13. Results of policy learning. The left two figures show average success rates (solid lines) and action mean-squared errors (dashed-dot lines) over training steps. Numeric entries indicate the optimal values across training steps. The rightmost figure shows the simulation results of iSD with NFE=2.

reflect the success rate, and iSD can achieve higher success rates despite yielding higher action errors than other methods.

We note that trigonometric interpolation underperforms linear interpolation under iSD settings, achieving an average success rate of 0.605 on Push-T with NFE=2. This is consistent with the observation that interpolation exhibits varying performance across settings, and that linear interpolation appears to be a more suitable choice for policy generation in this setting.

C.6. Loss Landscape

To assess the stability of iSD, we conduct loss landscape analysis with (Yao et al., 2020) on ImageNet-trained DiT-B/4. For each objective, we compute the top-2 eigenvectors of its Hessian to explore the landscape along the maximum curvature. To probe the earlier training stage, we compute the Hessian at 100K training steps. We measure the loss variance and count spikes by identifying outliers beyond a 95% confidence bound to validate the linearization cost hypothesis.

We observe that time-condition relaxation empirically reduces loss spikes and variance, supporting the linearization cost hypothesis. In Figure 14c, iSD shows even lower variance. After joint training with flow matching, as shown in the lower row, variances and spikes decrease, leading to more stable training and improved reproducibility.

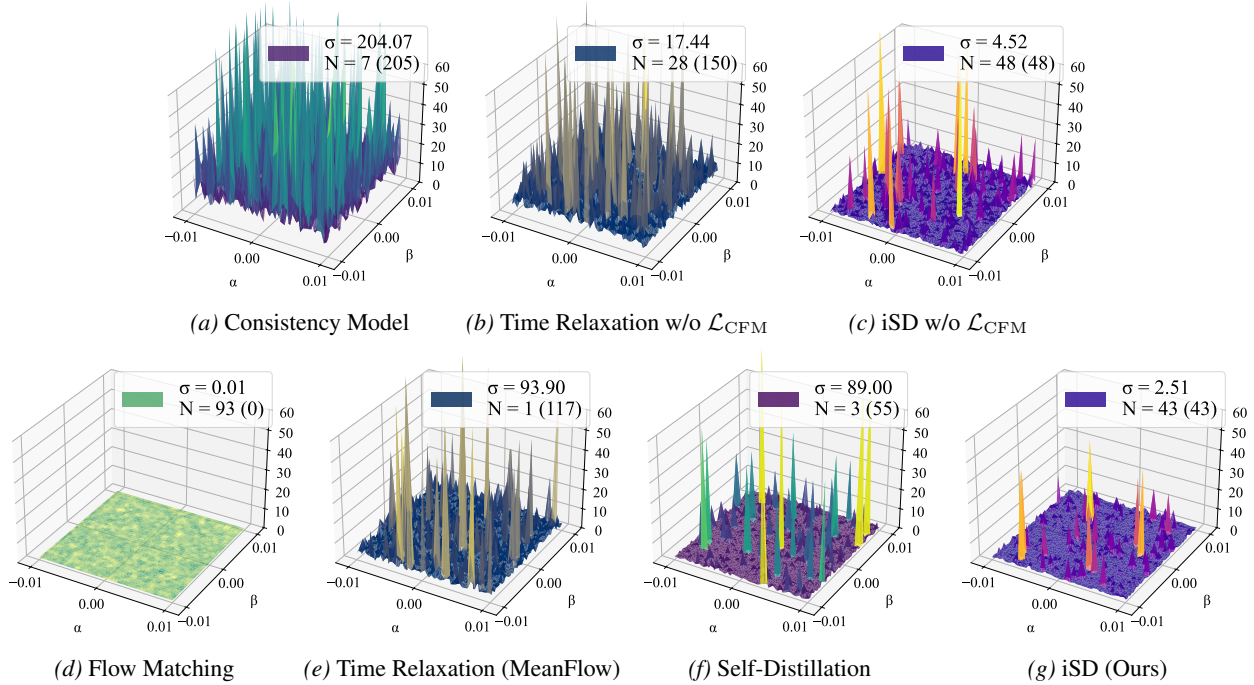


Figure 14. Loss landscapes of four methods. α and β denote the top-2 eigenvectors of the Hessian on ImageNet-1K with DiT-B/4. σ denotes the standard deviations of the landscape fields, and N the number of samples outside each method’s own 95% confidence bound. Values in parentheses report the number of samples exceeding the 95% bound defined by iSD, as a common reference.

Table 11. Quantitative results over training steps (2-NFE). The numeric entries in the header denote training steps. Reported results are averaged over three random seeds unless otherwise specified; entries marked with an underline are averaged over five seeds. *Std.* denotes the standard deviation at 400K steps (and at 800K steps for the bottom table). Hyphens in *Std.* indicate cases evaluated with a single run, where standard deviation was not computed. *HALTED* denotes cases where training diverged and was stopped earlier than the baseline.

(a) Frechet Inception Distance

LOSS	INTERP.	JVP	ARCH.	PRE-CFG ω	100K	200K	300K	400K	STD.
BASELINE	LINEAR	EXACT	DIT-B/4	-	137.84	127.23	122.76	120.49	<u>3.71</u>
JOINT-TRAINING	LINEAR	EXACT	DIT-B/4	-	132.84	105.90	94.94	101.29	<u>13.51</u>
\mathcal{L}_{CT}	LINEAR	EXACT	DIT-B/4	-	194.95	142.92	73.32	69.18	<u>2.71</u>
\mathcal{L}_{CT}	TRIG	EXACT	DIT-B/4	-	131.12	110.28	102.79	97.84	<u>3.40</u>
\mathcal{L}_{iSD}	LINEAR	EXACT	DIT-B/4	-	155.42	129.64	121.76	116.38	<u>1.10</u>
\mathcal{L}_{iSD}	TRIG	EXACT	DIT-B/4	-	147.01	125.83	117.19	110.18	<u>4.04</u>
\mathcal{L}_{CT}	LINEAR	APPROX	DIT-B/4	-	94.52	74.51	67.63	63.34	0.17
\mathcal{L}_{CT}	TRIG	APPROX	DIT-B/4	-	223.10	227.90	228.70	HALTED	-
\mathcal{L}_{iSD}	LINEAR	APPROX	DIT-B/4	-	144.27	120.69	112.35	108.13	<u>3.51</u>
\mathcal{L}_{iSD}	TRIG	APPROX	DIT-B/4	-	139.95	123.56	113.88	108.33	-
\mathcal{L}_{iSD-U}	LINEAR	APPROX	DIT-B/4	1.5	124.94	93.20	82.15	75.53	<u>1.48</u>
\mathcal{L}_{iSD-U}	TRIG	APPROX	DIT-B/4	1.5	119.86	86.21	74.48	67.66	<u>0.83</u>
\mathcal{L}_{iSD-C}	LINEAR	APPROX	DIT-B/4	1.5	166.93	128.24	110.30	100.47	-
\mathcal{L}_{iSD-C}	LINEAR	APPROX	DIT-B/4	3.0	200.17	120.56	98.73	88.93	-
\mathcal{L}_{iSD-C}	LINEAR	APPROX	DIT-B/4	7.0	270.50	HALTED	-	-	-
\mathcal{L}_{iSD-C}	TRIG	APPROX	DIT-B/4	1.5	164.34	133.90	119.94	111.56	-
\mathcal{L}_{iSD-C}	TRIG	APPROX	DIT-B/4	3.0	147.15	105.09	88.08	79.64	-
\mathcal{L}_{iSD-C}	TRIG	APPROX	DIT-B/4	7.0	192.14	127.65	111.93	110.49	-
\mathcal{L}_{iSD-T}	LINEAR	APPROX	DIT-B/4	1.5	115.18	83.02	70.88	63.81	-
\mathcal{L}_{iSD-T}	LINEAR	APPROX	DIT-B/4	3.0	61.77	39.68	31.80	27.62	-
\mathcal{L}_{iSD-T}	LINEAR	APPROX	DIT-B/4	5.0	55.22	37.21	31.04	27.49	<u>0.59</u>
\mathcal{L}_{iSD-T}	LINEAR	APPROX	DIT-B/4	7.0	51.88	36.85	31.46	28.61	-
\mathcal{L}_{iSD-T}	LINEAR	APPROX	DIT-B/4	10.0	54.90	41.77	37.07	33.86	-
\mathcal{L}_{iSD-T}	TRIG	APPROX	DIT-B/4	1.5	106.54	75.85	65.50	61.19	-
\mathcal{L}_{iSD-T}	TRIG	APPROX	DIT-B/4	3.0	46.01	24.35	18.42	15.56	-
\mathcal{L}_{iSD-T}	TRIG(OURS)	APPROX	DIT-B/4	5.0	40.36	22.11	17.28	15.20	<u>0.69</u>
\mathcal{L}_{iSD-T}	TRIG	APPROX	DIT-B/4	7.0	36.17	21.83	18.72	17.17	-
\mathcal{L}_{iSD-T}	TRIG	APPROX	DIT-B/4	10.0	40.54	25.69	21.75	20.18	-
MEANFLOW	LINEAR	EXACT	DIT-B/4	3.0	37.11	18.84	13.73	11.48	<u>1.68</u>
MEANFLOW	TRIG	EXACT	DIT-B/4	3.0	48.36	24.73	18.19	15.08	<u>3.11</u>
SHORTCUT MODEL	LINEAR	EXACT	DIT-B/4	1.5	96.02	81.74	77.51	87.52	<u>24.34</u>
FACFM	LINEAR	EXACT	DIT-B/4	1.75	59.45	39.41	30.79	25.52	<u>1.73</u>
\mathcal{L}_{iSD-U}	TRIG	APPROX	DIT-B/2	1.5	87.47	55.21	42.48	36.05	-
\mathcal{L}_{iSD-T}	TRIG	APPROX	DIT-B/2	3.0	36.40	19.20	13.83	11.92	-
\mathcal{L}_{iSD-T}	TRIG	APPROX	DIT-B/2	5.0	31.00	18.96	16.75	15.93	-
\mathcal{L}_{iSD-T}	TRIG	APPROX	DIT-L/2	3.0	26.02	14.86	12.11	11.17	-
\mathcal{L}_{iSD-U}	TRIG	APPROX	DIT-XL/2	1.5	87.47	55.21	42.48	36.05	-
\mathcal{L}_{iSD-T}	TRIG	APPROX	DIT-XL/2	3.0	24.69	14.33	11.82	11.08	-
\mathcal{L}_{iSD-T}	TRIG	APPROX	DIT-XL/2	5.0	28.30	18.89	17.33	17.03	-
\mathcal{L}_{iSD-T}	TRIG	APPROX	DIT-XL/2 [†]	3.0	14.53	5.82	4.30	3.79	-
\mathcal{L}_{iSD-T}	TRIG	APPROX	DIT-XL/1 [†]	3.0	7.15	3.01	2.64	2.52	-
LOSS	INTERP.	JVP	ARCH.	PRE-CFG ω	500K	600K	700K	800K	
\mathcal{L}_{iSD-U}	TRIG	APPROX	DIT-XL/2	1.5	30.87	27.56	24.80	23.40	
\mathcal{L}_{iSD-T}	TRIG	APPROX	DIT-XL/2	3.0	10.66	10.48	10.29	10.30	
\mathcal{L}_{iSD-T}	TRIG	APPROX	DIT-XL/2	5.0	16.87	16.85	16.96		
\mathcal{L}_{iSD-T}	TRIG	APPROX	DIT-XL/2 [†]	5.0	3.47	3.28	3.09	2.76	
\mathcal{L}_{iSD-T}	TRIG	APPROX	DIT-XL/1 [†]	5.0	2.40	2.26			

(b) Inception Score

LOSS	INTERP.	JVP	ARCH.	PRE-CFG ω	100K	200K	300K	400K	STD.
BASELINE	LINEAR	EXACT	DIT-B/4	-	7.90	8.88	9.40	9.69	<u>0.47</u>
JOINT-TRAINING	LINEAR	EXACT	DIT-B/4	-	10.95	13.01	14.32	12.70	<u>3.49</u>
\mathcal{L}_{CT}	LINEAR	EXACT	DIT-B/4	-	8.76	11.34	19.78	21.45	<u>1.15</u>
\mathcal{L}_{CT}	TRIG	EXACT	DIT-B/4	-	11.77	15.04	16.79	18.11	0.98
\mathcal{L}_{iSD}	LINEAR	EXACT	DIT-B/4	-	7.24	9.40	10.17	10.75	0.08
\mathcal{L}_{iSD}	TRIG	EXACT	DIT-B/4	-	9.37	12.02	13.53	14.75	0.70
\mathcal{L}_{CT}	LINEAR	APPROX	DIT-B/4	-	14.87	19.48	21.94	23.86	0.11
\mathcal{L}_{CT}	TRIG	APPROX	DIT-B/4	-	3.76	3.85	3.89	HALTED	-
\mathcal{L}_{iSD}	LINEAR	APPROX	DIT-B/4	-	8.48	10.71	11.49	11.91	0.39
\mathcal{L}_{iSD}	TRIG	APPROX	DIT-B/4	-	10.02	11.80	13.68	14.93	-
\mathcal{L}_{iSD-U}	LINEAR	APPROX	DIT-B/4	1.5	10.60	15.38	17.70	19.63	0.45
\mathcal{L}_{iSD-U}	TRIG	APPROX	DIT-B/4	1.5	12.72	20.71	25.57	29.26	0.52
\mathcal{L}_{iSD-C}	LINEAR	APPROX	DIT-B/4	1.5	6.45	9.33	11.18	12.54	-
\mathcal{L}_{iSD-C}	LINEAR	APPROX	DIT-B/4	3.0	4.88	10.16	12.55	13.98	-
\mathcal{L}_{iSD-C}	LINEAR	APPROX	DIT-B/4	7.0	1.83	HALTED	-	-	-
\mathcal{L}_{iSD-C}	TRIG	APPROX	DIT-B/4	1.5	8.04	10.95	12.58	13.88	-
\mathcal{L}_{iSD-C}	TRIG	APPROX	DIT-B/4	3.0	9.14	14.30	17.17	18.84	-
\mathcal{L}_{iSD-C}	TRIG	APPROX	DIT-B/4	7.0	4.69	10.79	12.42	13.12	-
\mathcal{L}_{iSD-T}	LINEAR	APPROX	DIT-B/4	1.5	11.87	17.14	20.84	23.85	-
\mathcal{L}_{iSD-T}	LINEAR	APPROX	DIT-B/4	3.0	24.94	41.33	53.74	63.90	-
\mathcal{L}_{iSD-T}	LINEAR	APPROX	DIT-B/4	5.0	28.52	47.35	60.49	72.20	<u>2.83</u>
\mathcal{L}_{iSD-T}	LINEAR	APPROX	DIT-B/4	7.0	31.42	50.69	63.81	75.09	-
\mathcal{L}_{iSD-T}	LINEAR	APPROX	DIT-B/4	10.0	28.87	42.85	53.79	63.18	-
\mathcal{L}_{iSD-T}	TRIG	APPROX	DIT-B/4	1.5	15.68	25.63	31.76	35.41	-
\mathcal{L}_{iSD-T}	TRIG	APPROX	DIT-B/4	3.0	39.45	84.45	114.30	135.60	-
\mathcal{L}_{iSD-T}	TRIG(OURS)	APPROX	DIT-B/4	5.0	46.56	102.97	143.55	181.24	<u>4.30</u>
\mathcal{L}_{iSD-T}	TRIG	APPROX	DIT-B/4	7.0	52.79	117.45	157.02	186.79	-
\mathcal{L}_{iSD-T}	TRIG	APPROX	DIT-B/4	10.0	46.28	100.12	137.87	164.59	-
MEANFLOW	LINEAR	EXACT	DIT-B/4	3.0	45.38	100.49	140.32	167.60	<u>20.39</u>
MEANFLOW	TRIG	EXACT	DIT-B/4	3.0	39.22	89.40	123.32	147.18	<u>22.16</u>
SHORTCUT MODEL	LINEAR	EXACT	DIT-B/4	1.5	13.58	15.75	16.25	14.94	<u>3.68</u>
FACFM	LINEAR	EXACT	DIT-B/4	1.75	24.05	39.32	52.87	65.42	<u>4.84</u>
\mathcal{L}_{iSD-U}	TRIG	APPROX	DIT-B/2	1.5	16.28	25.70	34.44	42.48	-
\mathcal{L}_{iSD-T}	TRIG	APPROX	DIT-B/2	3.0	44.96	93.25	132.21	156.90	-
\mathcal{L}_{iSD-T}	TRIG	APPROX	DIT-B/2	5.0	56.63	122.93	153.30	170.99	-
\mathcal{L}_{iSD-T}	TRIG	APPROX	DIT-L/2	3.0	61.29	122.22	159.68	178.42	-
\mathcal{L}_{iSD-U}	TRIG	APPROX	DIT-XL/2	1.5	16.28	25.70	34.44	42.48	-
\mathcal{L}_{iSD-T}	TRIG	APPROX	DIT-XL/2	3.0	64.95	127.97	165.02	185.29	-
\mathcal{L}_{iSD-T}	TRIG	APPROX	DIT-XL/2	5.0	66.44	140.28	179.87	201.29	-
\mathcal{L}_{iSD-T}	TRIG	APPROX	DIT-XL/2 [†]	3.0	97.80	172.30	204.08	219.71	-
\mathcal{L}_{iSD-T}	TRIG	APPROX	DIT-XL/1 [†]	3.0	200.26	278.90	295.43	304.74	-

LOSS	INTERP.	JVP	ARCH.	PRE-CFG ω	500K	600K	700K	800K
\mathcal{L}_{iSD-U}	TRIG	APPROX	DIT-XL/2	1.5	51.00	57.25	64.07	68.70
\mathcal{L}_{iSD-T}	TRIG	APPROX	DIT-XL/2	3.0	199.70	212.66	225.43	233.06
\mathcal{L}_{iSD-T}	TRIG	APPROX	DIT-XL/2	5.0	220.07	233.32	234.85	-
\mathcal{L}_{iSD-T}	TRIG	APPROX	DIT-XL/2 [†]	3.0	235.11	245.51	251.24	257.96
\mathcal{L}_{iSD-T}	TRIG	APPROX	DIT-XL/1 [†]	3.0	307.30	313.50	-	-

D. Qualitative Results

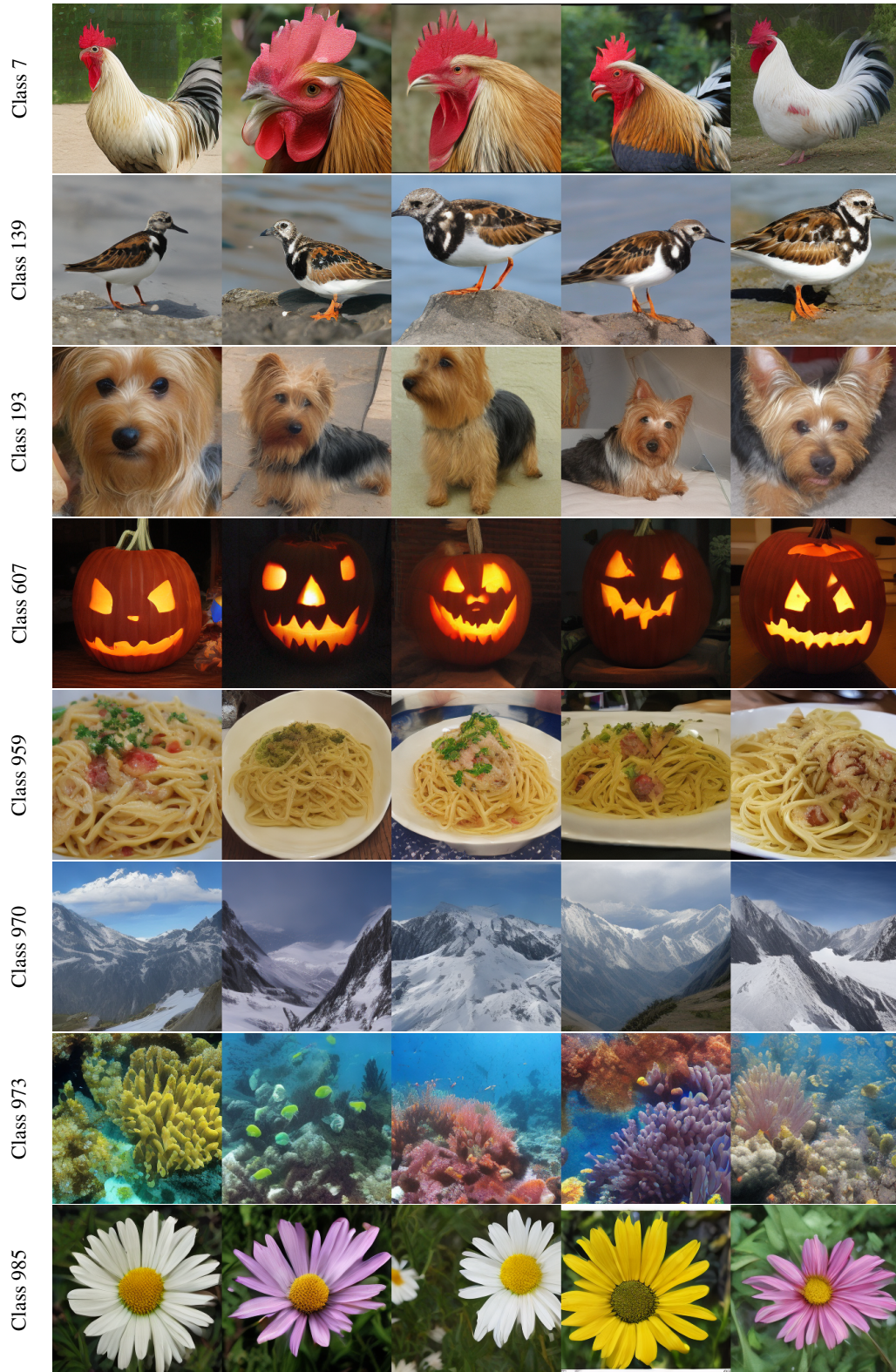


Figure 15. Class-level samples generated by iSD-T with two-step sampling on ImageNet 256×256.

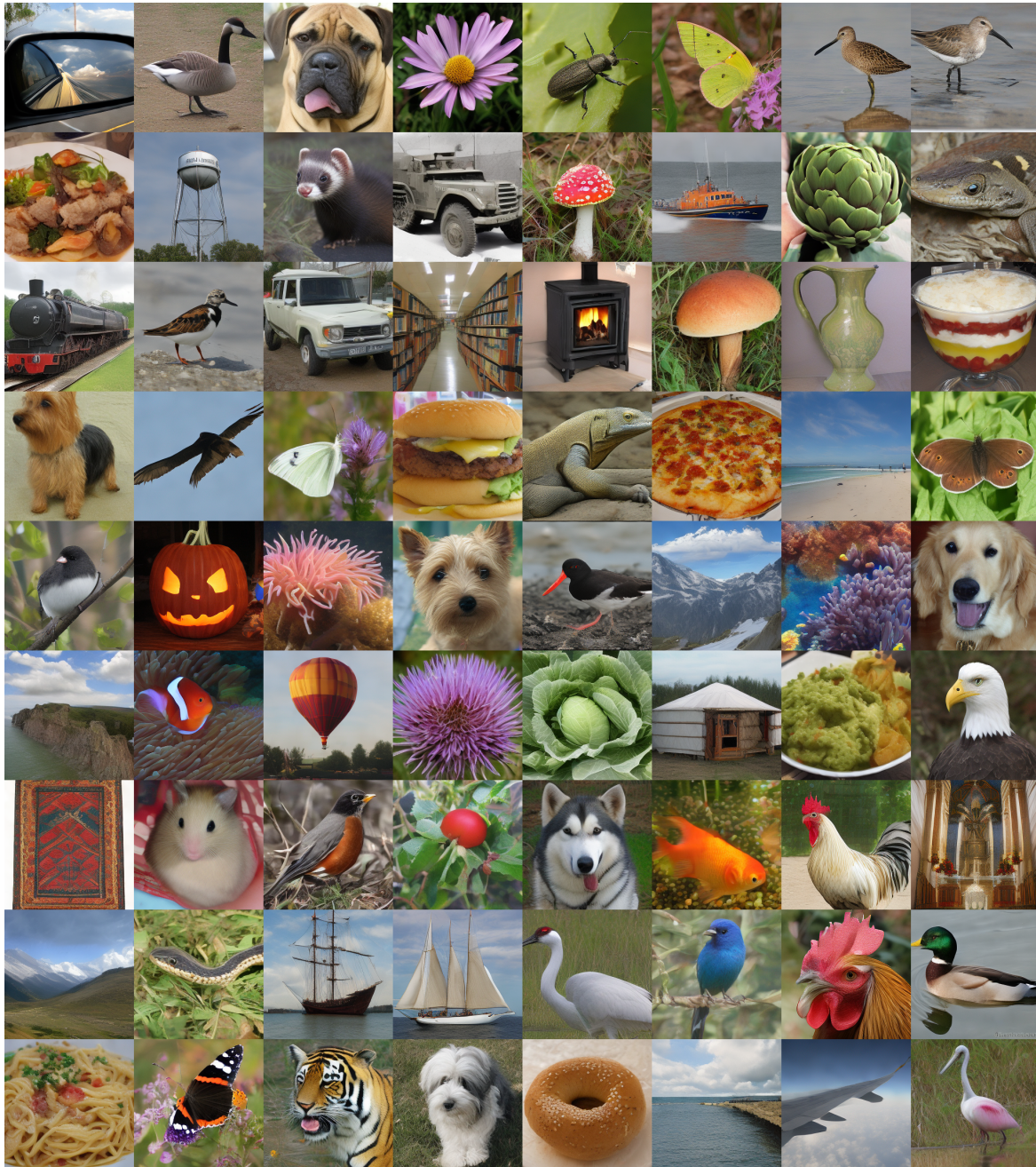


Figure 16. Two-step samples from the iSD-T on ImageNet 256 × 256.